

Molecular absorption lines at high redshift: PKS1413+135 ($z=0.247$)

T. Wiklind¹, F. Combes²

¹ Onsala Space Observatory, S-43992 Onsala, Sweden

² DEMIRM, Observatoire de Paris, 61 Av. de l'Observatoire, F-75014 Paris, France

Received date; Accepted date

Abstract. A detailed study of the absorbing molecular clouds towards the radio source PKS1413+135, at a redshift $z=0.247$, is reported. Physical conditions (density, temperature, filling factors) are derived for the molecular gas, in the frame work of two models: a homogeneous multicomponent model with equal filling factors, and a two-phase medium consisting of dense clumps embedded in a more diffuse component. It is shown that our absorption data are consistent with the presence of a diffuse gas component, dominating the observed opacity, and a dense component, accounting for most of the mass. We also show that without knowledge of the small scale structure of the absorbing molecular gas, we can only derive lower limits to the column density. Given the very narrow absorption spectrum, the size of the overall absorbing cloud along the line of sight must be quite small, of the order of 1 pc. The variability of the absorption spectrum has been studied over a time range of more than 2 years. We find that the opacity ratio between two absorbing components in CO has varied by a factor 2.3 ± 0.3 . The variations are interpreted as a change of the line of sight due to structural changes in the background source. We discuss what can be derived from molecular absorption line observations concerning the invariance of physical constants, such as the mass of the molecules. We discuss molecular line data from redshifts 0.27–0.89, corresponding to look-back times of 30% to 60% of the age of the universe.

Key words: interstellar medium: molecules – interstellar medium: clouds – galaxies: BL Lac objects individual: PKS1413+135 – galaxies: ISM – galaxies: quasars: absorption lines – radio continuum: galaxies

1. Introduction

Studies of absorption lines towards high redshift QSOs give detailed information about the interstellar medium (ISM) in distant objects at a linear resolution limited only by the size of the background continuum source. Absorption line observations also have a superior sensitivity compared to the corresponding emission lines and can successfully be used as probes of the composition as well as the physical and chemical conditions in the ISM. Such observations have for the most part been done at optical wavelengths, but the last few years have seen an increase in the number of high redshift absorption line systems observed at radio wavelengths.

The neutral atomic gas component has been observed through absorption of the 21 cm line of atomic hydrogen. About a dozen 21 cm HI absorbers at redshifts $z \gtrsim 0.2$ have been detected (Carilli 1995), with typical column densities $N(\text{HI}) = 5 \times 10^{18} (T_{\text{sp}}/f_{\text{HI}}) \text{ cm}^{-2}$ (e.g. Briggs 1988; Carilli 1995), where T_{sp} is the spin temperature in K and f_{HI} is the covering factor of atomic gas across the extent of the background continuum source.

Compared to the ionized and atomic parts of the ISM, the molecular gas component is characterized by high densities and low temperatures. Stars are formed directly from the molecular gas, and its physical and chemical status gives information about the stellar formation history as well as giving the initial conditions for the on-going star formation. We have recently detected absorption of molecular rotational transitions in four galaxies at redshifts 0.25–0.89 (Wiklind & Combes 1994, 1995, 1996a,b; Combes & Wiklind 1996). The background source is in all cases a highly obscured radio-loud QSO, located either in the background or in the galaxy where the absorption takes place. Absorptions in the millimeter wave band provide a velocity resolution more than two orders of magnitude higher than in optical spectroscopy. Since the amount of molecular gas needed to produce a detectable absorption line is less than $1 M_{\odot}$, the sensitivity of molec-

ular absorption line observations in terms of total mass is $\sim 10^{12}$ times higher than for the corresponding emission lines (cf. Wiklind & Combes 1994). This permits us to derive physical properties of the molecular component of the ISM at high redshifts which would otherwise be impossible.

In this paper we present new molecular absorption line data on the absorption system at $z=0.24671$ towards PKS1413+135. In Sect. 2 we give a general background to the radio source PKS1413+135 and the absorbing galaxy. The observations and data reduction are presented in Sect. 3. Our results are given in Sect. 4: in particular, we derive the physical properties of the molecular gas and we discuss possible time variations in the absorption lines. In Sect. 5 we compare the chemistry of the redshifted molecular gas with Galactic and nearby extragalactic systems and we discuss constraints to variations in physical constants derived from our absorption line data. Finally in Sect. 6 we summarize our results.

2. PKS1413+135 and the galaxy at $z=0.247$

The radio source PKS1413+135 has a flat continuum spectrum extending from a few hundred MHz into the near-infrared, with an exponential decrease at $\sim 5 \mu\text{m}$ (e.g. McHardy et al. 1991). The radio loud AGN is invisible at optical wavelengths. On the basis of this steep infrared to optical continuum, PKS1413+135 was originally classified as a red QSO (e.g. Bregman et al. 1981). The abrupt decrease of the continuum in the near-infrared was modeled as a high-energy cut-off in the electron energy distribution. Spectroscopic surveys in both the infrared and optical bands showed no prominent emission lines (Bregman et al. 1981; McHardy et al. 1994; Perlman et al. 1996). Stocke et al. (1992) detected Balmer absorption lines and weak [OII] 3727 Å emission at $z=0.247$. Rapid variability at radio and infrared wavelengths, strong and rapid variable infrared polarization and a flat-spectrum radio continuum, lead to a classification of PKS1413+135 as a BL Lac object. Subsequent radio imaging using VLBI techniques has questioned this classification. The radio source consists of: (1) a compact radio core, (2) a jet-like structure on a parsec scale, and (3) a counter-jet (Perlman et al. 1996). All the features except the compact core have steep spectral indices, meaning that their contribution to the continuum flux is negligible at millimeter wavelengths. The presence of a counter-jet disagrees with the interpretation of PKS1413+135 as a BL Lac object, since these are believed to represent radio sources with the jet pointing almost exactly along the line-of-sight, with the flux boosted by relativistic beaming. The counter-jet would not be visible in this scenario. Perlman et al. (1996) model PKS1413+135 as a typical Compact Symmetric Object (CSO); a young radio source with an age $\leq 10^4$ yrs. Doppler-boosting of the continuum could occur in the core, but not in the parsec scale jet and counter-jet.

Imaging of the system in optical and infrared bands reveals an edge-on galaxy (inclination $i \approx 87^\circ$) with a prominent dust lane (McHardy et al. 1991, 1994; Stocke et al. 1992). The luminosity profile is exponential with a scale length of $1.8''$, corresponding to 5.8 kpc for $H_0 = 75 \text{ km s}^{-1} \text{ Mpc}^{-1}$ and $q_0 = 0.5$ (these values are used throughout this paper). The disk-to-bulge ratio is ~ 1.1 (McHardy et al. 1994), but this value is uncertain due to unknown extinction corrections. The integrated blue luminosity (obtained from the V-band which approximately corresponds to the B-band in the restframe of the galaxy) is 19.6 ± 0.15 (McHardy et al. 1992), giving $M_B = -20.49$ or $L_B = 2.4 \times 10^{10} L_\odot$. No sign of the AGN is seen at optical wavelengths, but in the infrared the luminosity becomes dominated by a point source. This point source is situated within $0.1''$ (325 pc) of the center of the galaxy (Stocke et al. 1992). If the radio source is situated behind the galaxy, this close alignment would lead to gravitational lensing. No signs are found for image multiplicity or distortion, in either optical or radio bands (e.g. Stocke et al. 1992; Perlman 1996), strongly suggesting that the galaxy at $z=0.247$ is host to the radio source.

The X-ray spectrum shows a deficiency of low-energy X-ray photons, indicative of an extinction $A_V > 30 \text{ mag}$ (Stocke et al. 1992; McHardy et al. 1994). This corresponds to an absorbing screen with $N(\text{H}) > 10^{22} \text{ cm}^{-2}$. Carilli et al. (1992) detected redshifted 21 cm absorption at $z=0.24671$, with a column density $N(\text{HI}) = 1.3 \times 10^{19} (T_s/f_{\text{HI}})$, where T_s is the spin-temperature and f_{HI} is the covering factor of atomic gas across the background source. Wiklind & Combes (1994) reported molecular absorption at the redshift of the galaxy, with $N(\text{H}_2) = 4 \times 10^{20} \text{ cm}^{-2}$. These column densities are much smaller than that inferred from the X-ray data, but suggest that the galaxy at $z=0.247$ is of late type. The presence of molecular and atomic gas, the exponential luminosity profile and the broad-band colours are consistent with the galaxy being of morphological type Sb-c.

Hence, PKS1413+135 is a radio source situated in a spiral galaxy at a redshift $z=0.24671$. The blue luminosity of the galaxy is typical for an Sbc. The abrupt cut-off in the optical continuum is caused by extinction, and not by a cut-off in the electron energy distribution. An excess in near-infrared emission should be present due to dust heated by radiation from the AGN or by the interaction of the relativistic electrons with the ambient interstellar medium. No such excess has been observed (cf. Stocke et al. 1992).

3. Observations and data reduction

3.1. Observations

The observations presented in this paper have mainly been obtained at the IRAM (Institut de Radio Astronomie Millimétrique) 30-m telescope on Pico Veleta in Spain during

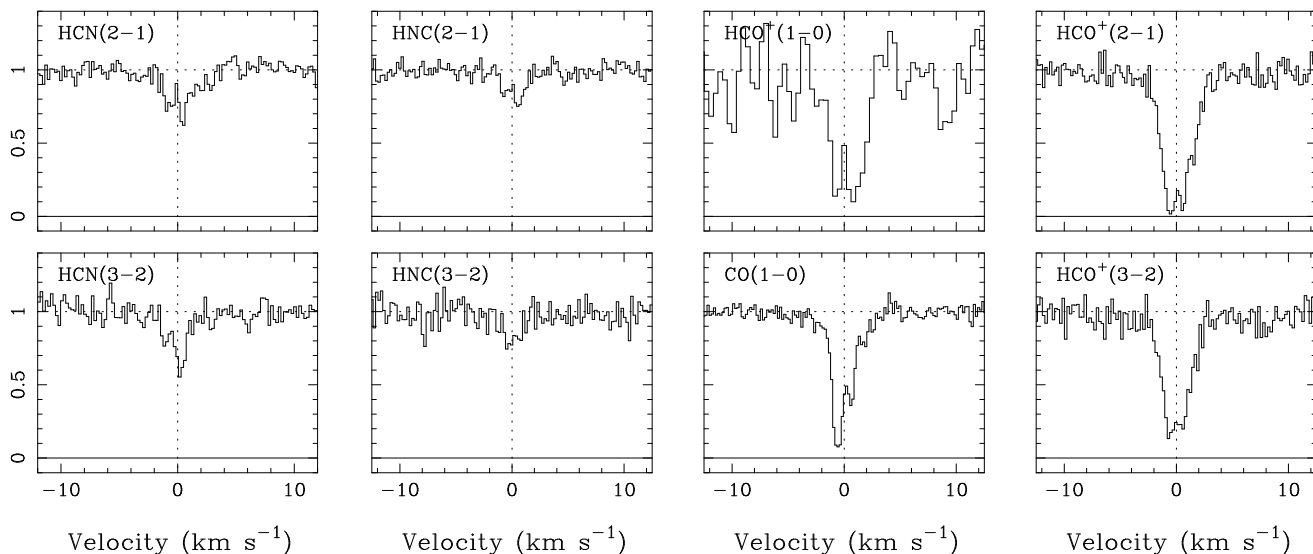


Fig. 1. Total averages of the $J=0\rightarrow1$ transitions of CO and HCO^+ , the $J=1\rightarrow2$ and $J=2\rightarrow3$ transitions of HCN, HCO^+ and HNC towards PKS1413+135. The velocity resolutions are $\sim 0.2 \text{ km s}^{-1}$ for all spectra. All transitions have been obtained with the IRAM 30-m telescope, except $\text{HCO}^+(0\rightarrow1)$ which was observed with the NRAO 12-m telescope at Kitt Peak. The continuum levels have been normalized to unity and zero velocity corresponds to a heliocentric redshift of 0.24671.

several observing runs from February 1994 to July 1996. Some absorption lines were also observed at the NRAO 12-m telescope at Kitt Peak¹ in February 1996.

At the IRAM 30-m telescope we used 3-, 2- and 1.3-mm SIS receivers, tuned to the redshifted frequencies of the molecular transitions in question (see Table 1). The observations were done with a nutating subreflector, switching symmetrically $\pm 90''$ in azimuth with a frequency of 0.5 Hz. The continuum levels of the observed sources were determined using a continuum backend and increasing the subreflector switch frequency to 2 Hz. The image sideband rejection of the receivers varied from 0 dB (double sideband) to 20 dB (single sideband), and was taken into account to determine the continuum temperatures T_c displayed in Table 2. The typical system temperature ranged from 200 K and up, depending on the whether conditions. Data obtained under bad weather conditions have been discarded. For the line observations we used broad filterbanks and narrow band autocorrelators, the former giving velocity resolutions $1\text{--}3 \text{ km s}^{-1}$, depending on the observed frequency, and a bandwidth of $500\text{--}1000 \text{ km s}^{-1}$. With the autocorrelators we chose frequency resolutions of 10 kHz for the 3-mm receiver, 20 kHz for the 2-mm and 40 kHz for the 1-mm receivers. The corresponding velocity resolutions are 30 m s^{-1} , 40 m s^{-1} and 50 m s^{-1} , respectively. The bandwidths for the autocorrelators were $40\text{--}50 \text{ km s}^{-1}$. The pointing of the telescope was checked regularly on the observed sources or on nearby continuum

sources. Since the weather was good and stable for most of the observations, we could monitor the continuum flux of the observed source during the integration to directly check the pointing of the telescope. Typical pointing corrections were $5\text{--}10''$.

At the NRAO 12-m telescope we used the SIS receiver for the lower part of the 3-mm band, tuned to the redshifted frequencies of the observed transitions. The receiver contains two mixers allowing dual polarization observations. For the lowest frequencies, only one of the mixers could be used due to high receiver temperatures in the other. Typical system temperatures were in the range 300–500 K. The observations were done with a dual chopping of the subreflector; the chopping was done at a rate of 1.25 Hz with a beamthrow of $2'$. As backends we used the filterbanks, giving spectral resolutions of 0.25 and 0.50 MHz. The pointing and focus were checked regularly on Venus and Saturn.

The data presented here is given in chopper-wheel calibrated antenna temperatures (T_A^*). The NRAO data is initially represented in the T_R^* scale. To transform it into the T_A^* temperature scale we multiplied the T_R^* values with the forward spillover and scattering efficiency, $\eta_{fss} = 0.68$.

3.2. Data reduction

Each spectrum is the average of several 5–10 minutes integrations with a calibration in-between. Individual spectra were inspected for interference and bad spectral baselines. The channel-to-channel noise rms was used as a weighting factor when adding individual spectra together. Usually no baseline corrections were applied, although a small set

¹ NRAO is a facility of the National Science Foundation, operated under cooperative agreement by Associated Universities Inc.

Table 1. Observed molecules and transitions

| Mol. | Transition | $\nu_{\text{rest}}^{\text{a)}$ GHz | $\nu_{\text{obs}}^{\text{b)}$ GHz | Det. ^{c)} | Tel. ^{d)} |
|---------------------------------|-------------------------------------|---------------------------------------|--------------------------------------|--------------------|--------------------|
| CO | 0→1 | 115.271204 | 92.460319 | Yes | I |
| ¹³ CO | 0→1 | 110.201370 | 88.393748 | No | I |
| HCN | 0→1 | 88.631847 | 71.092593 | No | K |
| | 1→2 | 177.261111 | 142.183115 | Yes | I |
| | 2→3 | 265.886180 | 213.270271 | Yes | I |
| HCO ⁺ | 0→1 | 89.188523 | 71.539109 | Yes | K |
| | 1→2 | 178.375065 | 143.076630 | Yes | I |
| | 2→3 | 267.557619 | 214.610951 | Yes | I |
| H ¹³ CO ⁺ | 1→2 | 173.506782 | 139.171726 | No | I |
| HNC | 1→2 | 181.324758 | 145.442611 | Yes | I |
| | 2→3 | 271.981067 | 218.159048 | Yes | I |
| N ₂ H ⁺ | 0→1 | 93.173400 | 74.735424 | No | K |
| | 1→2 | 186.344874 | 149.469302 | No | I |
| | 2→3 | 279.511671 | 224.199430 | No | I |
| CN | 0→1 | 113.490980 | 91.0323830 | Yes | I |
| CS | 1→2 | 97.980950 | 78.591613 | No | K |
| H ₂ CO | 1 _{1,1} → 2 _{1,2} | 140.839504 | 112.968937 | No | I |
| O ₂ | 1 ₀ → 1 ₁ | 118.750 | 95.251 | No | I |

a) The rest-frequency of the observed molecules taken from Lovas (1992).

b) Derived from $\nu_{\text{obs}} = \nu_{\text{rest}} / (1 + z_a)$.

c) Detection: Yes/No.

d) Telescope: I=IRAM, K=Kitt Peak 12-m.

of spectra obtained under less favourable weather conditions were corrected with a 3rd order polynomial. The continuum level was derived directly from the spectra, taking care to only include data obtained under stable weather conditions. At the IRAM telescope we also used a continuum backend and a fast chopping technique to derive T_c . This was done at all the observed frequencies. The accuracy of the continuum level is critical for the subsequent interpretation of the data (see below). The spectra have not been binned or smoothed except in the cases when adding together data obtained with different frequency resolutions. In these cases spectra are rebinned to correspond to the spectra with the lowest spectral resolution. The spectra presented here have their continuum level normalized to unity.

3.3. The continuum level

The observed continuum level T_c of the background source is an important quantity when deriving parameters from the absorption lines. It is, however, difficult to obtain T_c with an accuracy better than 10% in a single measurement, due to calibration uncertainties inherent in the atmospheric models used for the chopper-wheel method. The variance about the mean of the opacity can be obtained by differentiating Eq. (4) in Sect. 4.2 and is

$$\sigma_{\tau_\nu} \approx \frac{\exp(\tau_\nu) - 1}{T_c} \sigma_{T_c}, \quad (1)$$

where σ_{T_c} is the standard deviation of the observed continuum temperature and we have neglected the variance of T_{abs} , the measured depth of the absorption line, which generally is much smaller than that of the continuum temperature. For $\tau \ll 1$, $\sigma_{\tau_\nu}/\tau \approx \sigma_{T_c}/T_c$, which is usually small for finite values of τ and T_c . For $\tau \gg 1$, $\sigma_{\tau_\nu} \approx \exp(\tau)\sigma_{T_c}/T_c$ and we lose all information about the true opacity. In the critical opacity region ($\tau \gtrsim 1$), the error in our estimate of the opacity depends nonlinearly on the continuum level and the opacity itself.

More specifically, the important parameter when deriving the opacity of an absorption line seen towards an unresolved background source, is the line-to-continuum ratio. The values derived are therefore independent of the true value of the continuum level as long as the only variations in T_c originate in instantaneous pointing uncertainties. This is the situation under good weather conditions, where the average calibration uncertainty is the only parameter affecting the derived opacity. When the atmospheric conditions change between two calibrations (typically 5–10 minutes), we lose information about the continuum level and the line-to-continuum ratio ceases to be a good measure of the opacity. When this has been the case, we chose a period of acceptable atmospheric conditions and adopted the derived T_c from this period to scale the rest of the data. However, in this procedure we become sensitive to pointing errors. Fortunately, their variance was always lower than 20% of the beam-width.

The main uncertainty in the derived column densities, excitation temperatures and, to a lesser extent, abundance ratios, originates in the uncertainty of the continuum level. The nonlinear dependence makes it difficult to quantify the formal uncertainty. Formal errors presented here are therefore based on the assumption that T_c is correct. The relative errors in T_c are then to be multiplied by 1.3, 1.7 and 3.2 to obtain the relative errors induced on τ , when $\tau_\nu = 0.5$, 1 and 2 respectively.

4. Results

4.1. The observed absorption lines

Towards the radio source PKS1413+135 we have observed 18 different molecular rotational transitions of a total of

11 molecules. Of these we clearly detect 9 transitions of 5 different molecules; the $J=0\rightarrow1$ lines of CO, HCO^+ and CN^2 , the $J=1\rightarrow2$ and $J=2\rightarrow3$ lines of HCN, HCO^+ and HNC. The observed transitions with their rest-frequencies and corresponding redshifted frequencies are presented in Table 1. In Table 2 we list the observed integrated optical depths and the derived excitation temperatures and column densities. Notice that some of the column densities in Table 2 are modified after a more thorough analysis (Sect. 4.2.3). The final column densities are presented separately in Table 3.

The detected transitions are shown in Figs. 1 and 2. The continuum levels have been normalized to unity. All the spectra in Fig. 1 except $\text{HCO}^+(0\rightarrow1)$ are averages of the observing sessions in 1994 (cf. Sect. 3). The 1995 and 1996 data have not been used since there might be temporal changes in the absorption profiles (see Sect. 4.5). In order to show the weak $\text{CN}(0\rightarrow1)$ line, the scaling in Fig. 2 is different from that of Fig. 1. The CN hyperfine transitions which fall within the spectrometer are the $J=3/2-1/2$ with $F=1/2-3/2$, $F=3/2-3/2$, $F=1/2-1/2$, $F=5/2-3/2$ and $F=3/2-1/2$. Only the $F=5/2-3/2$ line is formally detected, possibly blended with the $F=3/2-1/2$ line. The height of the markings corresponds to the observed intensities in the Orion hot core (cf. Lovas 1992).

Some of our non-detected transitions are shown in Fig. 3. Since the isotopic lines of $^{13}\text{CO}(0\rightarrow1)$ and $\text{H}^{13}\text{CO}^+(1\rightarrow2)$ remain undetected at low noise levels, the corresponding ^{12}CO and H^{12}CO^+ lines are not saturated, despite absorption depths close to unity. This means that the derived column densities are not affected by saturation effects. The peak opacities for the $\text{CO}(0\rightarrow1)$ and $\text{HCO}^+(1\rightarrow2)$ lines are 2–3 (see Table 2).

The column density of CO is estimated to be approximately $2 \times 10^{16} \text{ cm}^{-2}$. With a Galactic CO to H_2 abundance ratio of 5×10^{-5} (e.g. van Dishoeck & Black 1987), the column density of molecular hydrogen towards PKS1413+135 at $z=0.24671$ is $\sim 4 \times 10^{20} \text{ cm}^{-2}$.

4.2. Derivation of physical parameters

In order to derive physical parameters from molecular absorption line data one must consider three uncertainties: (i) the covering factor of absorbing gas across the finite extent of the background continuum source, (ii) the excitation temperature of the molecular gas and (iii) if LTE conditions apply. The first uncertainty affects the determination of the velocity integrated optical depth while the second and the third also affects the derivation of column densities.

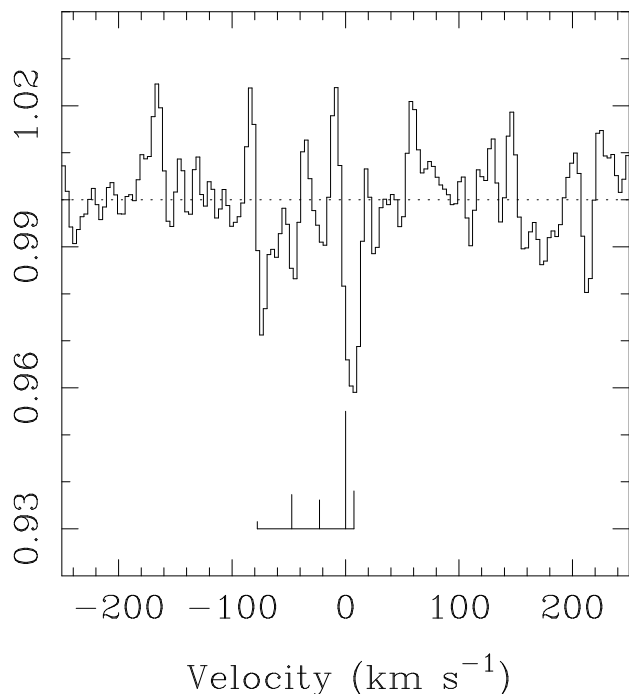


Fig. 2. Normalized spectra of CN $N=0\rightarrow1$ lines. From left to right we have indicated the $J=3/2-1/2$, $F=1/2-3/2$, $F=3/2-3/2$, $F=1/2-1/2$, $F=5/2-3/2$ and $F=3/2-1/2$ hyperfine transitions. Only the $F=5/2-3/2$ line is formally detected, possibly blended with the $F=3/2-1/2$ line. The height of the markings corresponds to the observed intensities in the Orion hot core (cf. Lovas 1992). The velocity resolution is 3.3 km s^{-1} and zero velocity corresponds to a heliocentric redshift of 0.2467.

4.2.1. Opacity

In a manner similar to Wiklind & Combes (1994) we express the observed continuum temperature, T_c , away from an absorption line as

$$T_c = f_s J(T_b), \quad (2)$$

where f_s is the beam filling factor of the region emitting continuum radiation, T_b is the brightness temperature of the background source and $J(T) = (h\nu/k)/[1 - \exp(-h\nu/kT)]$. The spatial extent of the region emitting continuum radiation at millimeter wavelengths is unknown. It is generally accepted that as the wavelength decreases, the emission originates from regions closer to the central AGN. At centimeter wavelengths, the core of PKS1413+135 is unresolved at milliarcsecond (mas) scales (Perlman et al. 1996). The core is likely to be smaller at millimeter wavelengths. The BL Lac 3C446 has been observed with mm-VLBI and has an extent $< 30 \mu\text{arcseconds}$ (Lerner et al. 1993). Since the angular size of the telescope beam is typically $25''$, the brightness temperature of the background source T_b is at least

² For CN we clearly detect one hyperfine transition: $N=1\rightarrow0$, $J=3/2-1/2$, $F=5/2-3/2$.

Table 2. Observed properties for PKS1413+135

| Molecule | Transition | $T_c^{(a)}$ mK | $\int \tau_\nu dV$ km s^{-1} | $\tau_0^{(b)}$ | $\sigma_\tau^{(c)}$ km s^{-1} | $\delta V^{(d)}$ km s^{-1} | Date(T) | $T_x^{(e)}$ K | N cm^{-2} |
|----------------------------|-------------------------------|-------------------|--|----------------|---|--|----------|----------------------|--------------------------------------|
| CO | 0 \rightarrow 1 | 1000 | 3.64 ± 0.06 | 2.8 | 0.063 | 0.06 | Total | 10^{+2}_{-2} | $2.3^{+0.8}_{-0.7} \times 10^{16}$ |
| | 0 \rightarrow 1 | 240 | 3.07 ± 0.11 | 2.5 | 0.077 | 0.13 | Apr95(I) | | |
| | 0 \rightarrow 1 | 495 | 3.62 ± 0.12 | >2.0 | 0.138 | 0.06 | May94(I) | | |
| | 0 \rightarrow 1 | 338 | 3.78 ± 0.08 | >2.4 | 0.097 | 0.06 | Mar94(I) | | |
| | 0 \rightarrow 1 | 230 | 3.08 ± 0.36 | >1.4 | 0.290 | 0.13 | Feb94(I) | | |
| | | | | | | | | | |
| ^{13}CO | 0 \rightarrow 1 | 1000 | <0.14 | <0.04 | 0.043 | 0.10 | Total | 10^{+2}_{-2} | $< 9.2^{+1.1}_{-2.8} \times 10^{14}$ |
| | 0 \rightarrow 1 | 240 | <0.23 | <0.06 | 0.019 | 1.06 | Apr95(I) | | |
| | 0 \rightarrow 1 | 512 | <0.19 | <0.07 | 0.022 | 0.72 | May94(I) | | |
| | | | | | | | | | |
| HCN | 0 \rightarrow 1 | 75 | <0.92 | 0.06 | 0.063 | 2.08 | Feb96(K) | | |
| | 1 \rightarrow 2 | 1000 | 0.99 ± 0.07 | 0.5 | 0.042 | 0.21 | Total | $11.8^{+3.1}_{-2.1}$ | $7.3^{+2.7}_{-1.5} \times 10^{12}$ |
| | 1 \rightarrow 2 | 170 | 1.52 ± 0.14 | 0.6 | 0.077 | 0.21 | Apr95(I) | | |
| | 1 \rightarrow 2 | 320 | 1.36 ± 0.11 | 0.6 | 0.079 | 0.16 | May94(I) | | |
| | 1 \rightarrow 2 | 243 | 0.46 ± 0.10 | 0.4 | 0.079 | 0.24 | Mar94(I) | | |
| | 3 \rightarrow 2 | 1000 | 0.93 ± 0.10 | 0.6 | 0.063 | 0.22 | Total | $11.8^{+3.1}_{-2.1}$ | $7.3^{+1.1}_{-0.3} \times 10^{12}$ |
| | 2 \rightarrow 3 | 120 | 0.95 ± 0.53 | 0.4 | 0.233 | 0.33 | Apr95(I) | | |
| | 2 \rightarrow 3 | 173 | 1.53 ± 0.19 | 0.8 | 0.135 | 0.16 | May94(I) | | |
| | 2 \rightarrow 3 | 146 | 0.80 ± 0.10 | 0.6 | 0.085 | 0.16 | Mar94(I) | | |
| | | | | | | | | | |
| HCO^+ | 0 \rightarrow 1 | 46 | 5.20 ± 0.50 | 1.5 | 0.218 | 0.41 | Feb96(K) | $5.4^{+0.7}_{-0.5}$ | |
| | 1 \rightarrow 2 | 1000 | 6.87 ± 0.06 | >2.6 | 0.079 | 0.04 | Total | $8.7^{+0.2}_{-0.2}$ | $2.9^{+0.1}_{-0.2} \times 10^{13}$ |
| | 1 \rightarrow 2 | 170 | 5.57 ± 0.19 | >2.0 | 0.131 | 0.21 | Apr95(I) | | |
| | 1 \rightarrow 2 | 340 | 7.22 ± 0.11 | >2.7 | 0.070 | 0.12 | May94(I) | | |
| | 1 \rightarrow 2 | 242 | 6.20 ± 0.15 | >2.3 | 0.108 | 0.16 | Mar94(I) | | |
| | 1 \rightarrow 2 | 128 | 4.51 ± 0.32 | >1.4 | 0.268 | 0.12 | Feb94(I) | | |
| | 2 \rightarrow 3 | 1000 | 4.75 ± 0.10 | 2.0 | 0.122 | 0.06 | Total | $8.7^{+0.2}_{-0.2}$ | $2.9^{+0.05}_{-0.05} \times 10^{13}$ |
| | 2 \rightarrow 3 | 120 | 5.98 ± 0.19 | 2.3 | 0.085 | 0.32 | Apr95(I) | | |
| | 2 \rightarrow 3 | 172 | 4.01 ± 0.18 | 1.3 | 0.172 | 0.11 | May94(I) | | |
| | 2 \rightarrow 3 | 144 | 4.72 ± 0.37 | >1.6 | 0.230 | 0.22 | Mar94(I) | | |
| H^{13}CO^+ | 1 \rightarrow 2 | 329 | <0.18 | <0.08 | 0.027 | 0.42 | May94(I) | $8.7^{+0.2}_{-0.2}$ | $< 7.9^{+0.1}_{-0.2} \times 10^{11}$ |
| HNC | 1 \rightarrow 2 | 1000 | 0.53 ± 0.05 | 0.3 | 0.040 | 0.21 | Total | $15.5^{+9.5}_{-5.0}$ | $5.2^{+5.7}_{-2.0} \times 10^{12}$ |
| | 1 \rightarrow 2 | 170 | 0.68 ± 0.11 | 0.3 | 0.043 | 0.41 | Apr95(I) | | |
| | 1 \rightarrow 2 | 310 | 0.69 ± 0.09 | 0.3 | 0.078 | 0.12 | May94(I) | | |
| | 1 \rightarrow 2 | 238 | 0.45 ± 0.07 | 0.2 | 0.054 | 0.16 | Mar94(I) | | |
| | 2 \rightarrow 3 | 1000 | 0.60 ± 0.11 | 0.3 | 0.085 | 0.21 | Total | $15.5^{+9.5}_{-5.0}$ | $5.2^{+3.2}_{-0.9} \times 10^{12}$ |
| | 2 \rightarrow 3 | 120 | 0.93 ± 0.29 | — | 0.127 | 0.32 | Apr95(I) | | |
| | 2 \rightarrow 3 | 168 | 0.78 ± 0.18 | 0.4 | 0.114 | 0.21 | May94(I) | | |
| | | | | | | | | | |
| CS | 1 \rightarrow 2 | 80 | < 0.62 | <0.21 | 0.048 | 1.88 | Feb96(K) | 10^{+2}_{-2} | $< 2.0^{+0.7}_{-0.6} \times 10^{13}$ |
| $\text{CN}^{(b)}$ | 0 \rightarrow 1 | 1000 | 1.10 ± 0.23 | 0.1 | 0.012 | 3.29 | Total | 10^{+2}_{-2} | $2.0^{+1.2}_{-1.1} \times 10^{13}$ |
| | 0 \rightarrow 1 | 240 | < 0.19 | <0.03 | 0.031 | 1.03 | Apr95(I) | | |
| | 0 \rightarrow 1 | 341 | < 0.15 | <0.01 | 0.014 | 3.29 | Mar94(I) | | |
| | 0 \rightarrow 1 | 150 | 1.10 ± 0.23 | 0.1 | 0.012 | 3.29 | Jul96(I) | | |
| N_2H^+ | 0 \rightarrow 1 | 075 | < 1.07 | <0.10 | 0.103 | 1.00 | Feb96(K) | 10^{+2}_{-2} | $< 9.9^{+3.7}_{-3.1} \times 10^{12}$ |
| | 1 \rightarrow 2 | 170 | < 0.48 | <0.03 | 0.028 | 2.00 | Apr95(I) | 10^{+2}_{-2} | $< 2.1^{+0.5}_{-0.4} \times 10^{12}$ |
| | 2 \rightarrow 3 | 120 | < 1.1 | <0.08 | 0.077 | 1.34 | Apr95(I) | 10^{+2}_{-2} | $< 6.3^{+0.3}_{+0.3} \times 10^{12}$ |
| H_2CO | $1_{1,1} \rightarrow 2_{1,2}$ | 296 | < 0.14 | <0.03 | 0.031 | 0.55 | Mar94(I) | 10^{+2}_{-2} | $< 1.5^{+1.3}_{-1.0} \times 10^{13}$ |
| O_2 | $1_0 \rightarrow 1_1$ | 484 | < 0.14 | <0.03 | 0.031 | 0.55 | May94(I) | 10^{+2}_{-2} | $< 2.0^{+0.7}_{-0.6} \times 10^{16}$ |

a) The continuum level in mK. Total averages have $T_c = 1000$ mK.

b) The maximum optical depth. A lower limit is set when the absorption reaches within the spectral noise rms of the zero level.

c) Channel-to-channel noise rms of the opacity.

d) Channel separation used for the derivation of opacities.

e) Derived or assumed excitation temperature in K.

f) Derived for an upper limit to the $N = 1 - 0$, $J = 3/2 - 1/2$, $F = 5/2 - 3/2$ line.

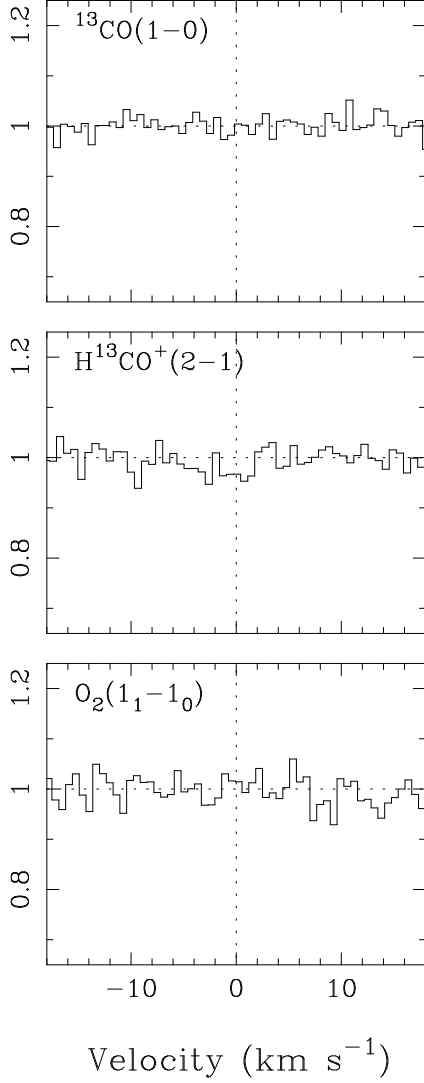


Fig. 3. Normalized spectra of the non-detected $^{13}\text{CO}(1\rightarrow0)$, $\text{H}^{13}\text{CO}^+(1\rightarrow2)$ and $\text{O}_2(1_0 \rightarrow 1_1)$ lines. The velocity resolution is 0.65, 0.66 and 0.64 km s^{-1} , respectively. The velocity scale is heliocentric. Notice the different scale for the continuum level compared with Fig. 1.

$10^9 \times T_c$. This means that we do not have to consider the local excitation temperature of the molecular gas when deriving the opacity, since this is typically of the order 10 K. The excitation does enter, however, when deriving column densities.

The observed antenna temperature of an absorption line can be expressed as

$$\Delta T_A^*(\nu) = f_s J(T_b) \{1 - f_c [1 - \exp(-\tau_\nu)]\}, \quad (3)$$

where f_c is the fraction of the continuum source area covered by molecular gas at the velocity corresponding to the frequency ν . We here assume that f_c is a characteristic covering factor for the molecular gas, independent of the

opacity τ_ν of the gas. $\Delta T_A^* = T_c - |T_{\text{abs}}|$, where T_{abs} is the depth of the absorption line measured from the continuum level. When τ_ν is very large the absorption saturates, i.e. $T_{\text{abs}}^* \rightarrow T_c$ and $\Delta T_A^* \rightarrow 0$. In this equation, we cannot derive independently the covering factor of the absorbing clouds, f_c , and their optical depth. Combining Eqs (1) and (2) we can express the ‘true’ optical depth as:

$$\tau_\nu = -\ln\left[1 - \frac{1}{f_c}(1 - \exp(-\tau_{\nu_{\text{obs}}}))\right], \quad (4)$$

where

$$\tau_{\nu_{\text{obs}}} = \ln\left(\frac{T_c}{\Delta T_A^*}\right).$$

$\tau_{\nu_{\text{obs}}}$ is the optical depth averaged over the size of the background continuum source and over the excitation conditions of the molecular gas along the line of sight. This value is given for each observed absorption line in Table 2. By assuming that the opacity of the absorbing gas is high, Eq. (3) gives a minimum possible value for the covering factor $f_c \gtrsim 1 - \exp(-\tau_{\nu_{\text{obs}}})$. Should the opacity be low, the filling factor must be even larger. The velocity integrated opacity is obtained by integrating τ_ν in Eq.(4) over the full extent of the absorption line.

In PKS1413+135 the optical depth of the $\text{CO}(0\rightarrow1)$ and $\text{HCO}^+(1\rightarrow2)$ lines is ~ 3 . This means that the absorption almost reaches the zero level, but it is not heavily saturated. The HCN, HNC and the $J=2\rightarrow3$ line of HCO^+ all have smaller optical depths. The non-detections of less abundant molecules such as CS, N_2H^+ and the isotopic variants ^{13}CO and H^{13}CO^+ are consistent with the detected lines not being heavily saturated. The large depth of the $\text{CO}(0\rightarrow1)$ and $\text{HCO}^+(1\rightarrow2)$ lines then implies that the covering factor f_c must be very close to unity. In the following we will set $f_c = 1$ for PKS1413+135.

4.2.2. Excitation temperature and column density

The excitation temperature T_x relates the relative population of two rotational levels of a molecule as:

$$\frac{n_2}{n_1} = \frac{g_2}{g_1} \exp(-h\nu_{21}/kT_x), \quad (5)$$

where g_i is the statistical weight for level i and $h\nu_{21}$ is the energy difference between two rotational levels. In order to derive T_x we must link the fractional population in level i to the total abundance (here abundance is used in synonym with column density). This is done by invoking a weak LTE-approximation and assuming that $T_x = T_{\text{rot}}$, where T_{rot} is a temperature which governs the fractional population of all rotational levels in a given molecule. The LTE approximation is weak in the sense that it does not imply that T_{rot} equals the kinetic temperature and it allows for different molecules to have different T_{rot} . With this approximation we can use the partition

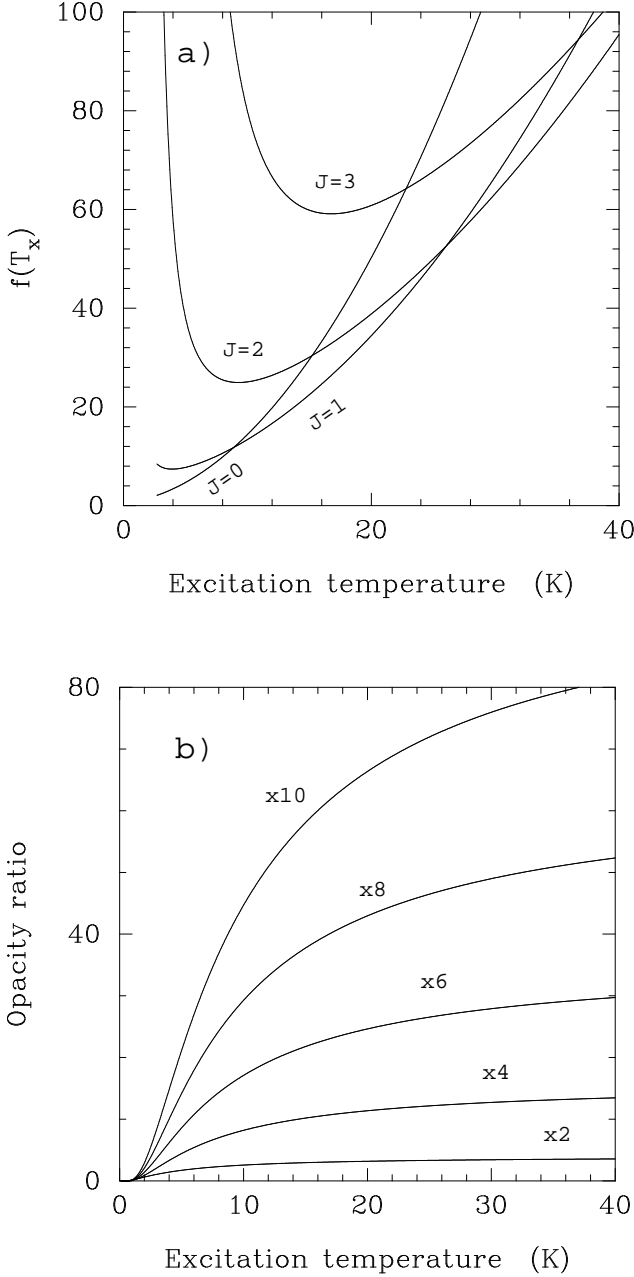


Fig. 4. a) The function $f(T_x)$ for the 4 lowest rotational transitions of HCO^+ as a function of the excitation temperature T_x (cf. Eq. 6). **b)** The ratio of integrated optical depth for the $J=1 \rightarrow 2$ line of HCO^+ for two different excitation temperatures, T_1 and T_2 . The number at each line in the plot corresponds to the factor a , $T_2 = aT_1$. The results show that for a given transition and equal column densities, the coldest gas component contributes the largest part of the observed opacity.

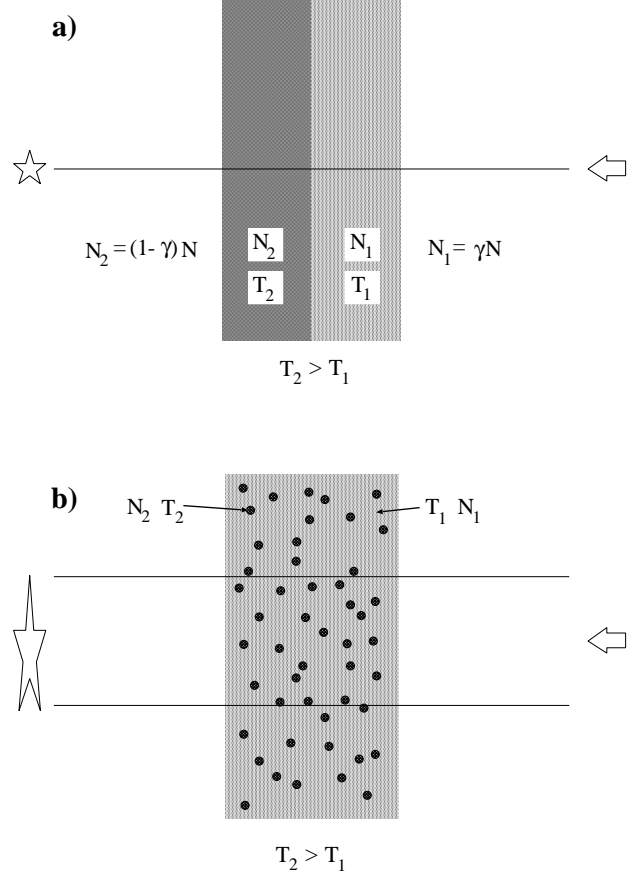


Fig. 5. a) A schematic illustration of a two-component molecular medium seen in absorption. The two components are characterized by excitation temperatures T_1 and T_2 , with $T_2 > T_1$ and represents a fraction γ and $1-\gamma$ of the total column density N (see the text for more details); **b)** Same as a) but with the warmer (denser) gas distributed in a clumpy medium. The line of sight is shown 'extended' to emphasize the clumpiness present within the gas causing the absorption profile.

function $Q(T_x) = \sum_{J=0}^{\infty} g_J \exp(-E_J/kT_x)$ to express the total column density N_{tot} as

$$N_{\text{tot}} = \frac{8\pi}{c^3} \frac{\nu^3}{g_J A_{J,J+1}} f(T_x) \int \tau_\nu dV, \quad (6)$$

$$f(T_x) = \frac{Q(T_x) \exp(E_J/kT_x)}{1 - \exp(-h\nu/kT_x)},$$

where $\int \tau_\nu dV$ is the observed optical depth integrated over the line for a given transition, $g_J = 2J + 3$ for a transition $J \rightarrow J + 1$ and E_J is the energy of the rotational level J . By taking the ratio of two observed transitions from the same molecule, the excitation temperature can be derived. If the lower transition is saturated, T_x will be an upper limit. Non-saturated lines will directly give T_x , limited only by the S/N in the spectra. The derivation of

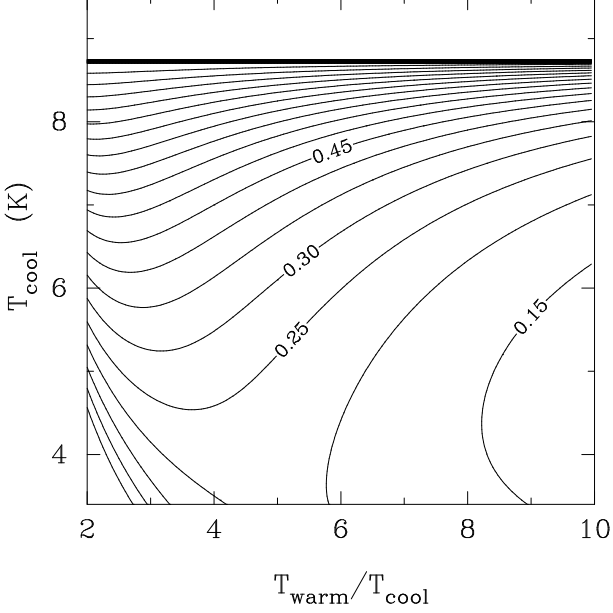


Fig. 6. The fraction γ of cool molecular gas in a two-component model, covering both all the continuum surface, of the molecular gas along the line of sight to PKS1413+135. The fraction is derived from the ratio of the $J=1\rightarrow2$ and $J=2\rightarrow3$ transitions of HCO^+ .

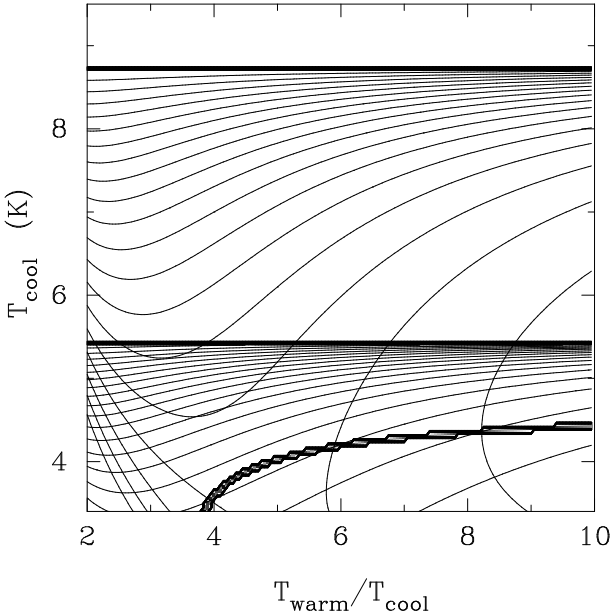


Fig. 7. The same fraction γ as in Fig. 6, but now including solutions also for the $J=0\rightarrow1/J=1\rightarrow2$ ratio. The grey-scaled area in the lower part of the figure represents the region where the two solutions agree, suggesting $\gamma = 0.2$, $T_{\text{cool}} = 4.2$ K and $T_{\text{warm}} \approx 25 - 30$ K.

the excitation temperature depends only on the line-to-continuum ratio of the two transitions in question and is therefore independent of a correctly measured continuum level, as long as this is not caused by changing weather conditions in between two calibrations. The T_x derived in this way is an average excitation temperature along the line of sight and averaged over the finite extent of the continuum source. The strong frequency dependence of the column density in Eq. (6) is only apparent since the Einstein coefficient $A_{J,J+1}$ is proportional to ν^3 .

4.3. Multicomponent analysis

Towards PKS1413+135 we have observed three transitions of HCO^+ which allows us to derive the excitation temperature using the ratio of the observed integrated opacities for the $J=0\rightarrow1/J=1\rightarrow2$ and $J=1\rightarrow2/J=2\rightarrow3$ lines. If weak-LTE conditions apply, as defined above, these ratios should give the same excitation temperature. This, however, is not the case. The first ratio gives $T_x = 5.4^{+0.7}_{-0.5}$ K, the second $8.7^{+0.2}_{-0.2}$ K. Is this an indication that the assumption of LTE conditions are at fault?

The above derivation of the excitation temperature and column density corresponds to values averaged over the angular extent of the background source as well as along the line of sight. Since these extents are both finite, we may well have several gas components characterized by different excitation temperatures contributing to the observed absorption lines.

The observed property of a molecular absorption line is the velocity integrated optical depth $\int \tau_\nu dV$, which is proportional to $N_{\text{tot}}/f(T_x)$ (e.g. Eq. 6). As shown in Fig. 4a, the function $f(T_x)$ is highly nonlinear. The ratio of the integrated opacities for a given molecule and transition will therefore depend strongly on the excitation temperature. The ratio of opacities of two gas components characterized by excitation temperatures $T_1 < T_2$ is shown in Fig. 4b for $\text{HCO}^+(1\rightarrow2)$, for T_2/T_1 ratios of 2–10. It is evident from the figure that the ‘cool’ gas component contributes significantly more to the opacity than the ‘warm’ gas. Note that the temperature refers to the excitation conditions, an excitationally cold gas can still be kinetically warm if the density is low enough. It is thus possible to combine a relatively large column of warm (i.e. dense) molecular gas with smaller column of excitationally cold (i.e. diffuse) gas to produce the observed opacity. In order to see how such a two-component medium can combine and still be consistent with the observed data, we express the opacity as:

$$\int \tau_\nu dV = \frac{c^3}{8\pi} \frac{A_{J,J+1} g_{J+1}}{\nu^3} N_{\text{tot}} \left[\frac{\gamma}{f(T_1)} + \frac{1-\gamma}{f(T_2)} \right], \quad (7)$$

where γ is the fraction of the total column density characterized by a temperature T_1 and $1 - \gamma$ is the fraction associated with gas of a temperature T_2 . In the following

we will assume that $T_1 < T_2$ and that the covering factor of the two components are equal. A schematic view of this two-component model is shown in Fig. 5a. In the next section we will study the case when the assumption of equal filling factors is relaxed. Taking the ratio of two observed opacities the column density is eliminated and we can solve for γ as a function of T_1 and T_2 . One result obtained for the $J=1 \rightarrow 2$ and $J=2 \rightarrow 3$ lines of HCO^+ is shown in Fig. 6. The ratio of the observed opacities give an average excitation temperature of 8.7 K (see Table 2), which is the limit for $\gamma = 1$ in Fig. 6. It is, however, possible to have a fraction $\gamma < 1$ of the total column density in the form of significantly colder gas, with the remaining $1 - \gamma$ in the form of a warmer gas component. The x -axis in Fig. 6 shows the ratio of the two temperatures. Hence, one solution is to have 25% of the column density in the form of a gas component with $T_x \approx 5$ K and 75% in the form of a warm gas component with $T_x \approx 20$ K.

By including all three transitions observed for HCO^+ , we get two sets of solutions for the fraction γ . These are shown in Fig. 7. The grey-scaled area indicates where the two solutions coincide. The results suggests the presence of an excitationally cold component with $T_x \approx 4$ K which constitutes a fraction $\sim 20\%$ of the total column density. The remaining 80% is made up of a gas with a $T_x \approx 20 - 40$ K. Hence, the non-concordant values of the excitation temperatures derived from three transitions of HCO^+ do not necessarily imply that the assumption of weak-LTE is violated, but are consistent with the presence of two gas components with different excitation temperatures.

There might be more than two gas components along the line of sight. By making the ansatz that we have N components, each characterized by an excitation temperature T_i , with $T_1 < T_2 < \dots < T_N$, the fraction γ of the coldest gas component will be somewhat smaller than derived assuming a 2-component model. However, the strong nonlinear behaviour of the opacity as a function of T_x (Fig. 4a,b), ensures that a third, fourth or higher gas component will give a small or negligible contribution to the observed opacity. *Thus, a 2-component model should give a reasonable approximation to the possible gas components existing along the line of sight and over the finite extent of the background source.*

Adopting values for T_1 and T_2 , giving a fraction γ , the total column density N can be derived. This value is always larger than for the ‘average’ T_x , with a maximum for the smallest allowed fraction γ of cold gas. This is a natural consequence of the nonlinear dependence of the opacity to the excitation temperature as shown in Fig. 4a. In the case of HCO^+ , the allowed solutions give total column densities in the range $3.7 - 11.2 \times 10^{13} \text{ cm}^{-2}$, with corresponding excitation temperatures 3.4 & 13.3 K and 4.5 & 44.5 K for the cold and warm components. The fraction γ is 0.19 and 0.12 for these two cases. The column density derived using the average T_x as given in Table 2 is $2.9 \times 10^{13} \text{ cm}^{-2}$. The maximum allowed fraction of cold

gas is $\gamma = 0.22$, with excitation temperatures 3.9 & 18.0 K and a total column density of HCO^+ of $4.5 \times 10^{13} \text{ cm}^{-2}$.

4.4. A clumpy medium

Since the excitation of molecular gas is generally governed by collisions with H_2 , a high- T_x gas is characterized by a high density. The division in cool and warm gas made in the previous section is therefore equivalent to a division into diffuse and dense gas. A more realistic multi-phase medium combining the dense and diffuse phases is that observed in the Milky Way ISM, where a clumpy structure of small and dense clouds with a small filling factor is embedded in a pervasive diffuse molecular medium. A schematic view of this two-component model is shown in Fig. 5b.

If we call f_c the area filling factor of each clump, for which $\tau_\nu \gg 1$, their contribution to the absorption depth is simply f_c (assuming that the brightness temperature of the background source is homogeneous over its extent). If we assume that there are in total n_c clouds in the beam, and that their line-width is δv each, corresponding to a velocity filling factor $f_v = \delta v / \Delta V$ (where ΔV is the total spectrum line-width observed), and neglecting cloud overlapping for the sake of simplicity, their combined contribution to the opacity, at a given ν , will be

$$n_c f_v f_c = 1 - \exp(-\tau_{\text{obs}}), \quad (8)$$

where τ_{obs} is the observed opacity. The total H_2 column density in the beam is then

$$N_{\text{H}_2} = \frac{4}{3} n_{\text{H}_2} r_c \frac{1 - \exp(-\tau_{\text{obs}})}{f_c f_v} \text{ cm}^{-2}, \quad (9)$$

where n_{H_2} is the density of molecular hydrogen in each clump and r_c the characteristic radius of the clumps. In order to see how the presence of small dense structures influence the derivation of column density we can use the simple parametrization presented above, together with the characteristic values derived from observations of the Galactic molecular ISM. Assuming a $\tau_{\text{obs}} = 0.5$ for the $\text{CO}(0 \rightarrow 1)$ line a velocity width $\delta v = 0.1 \text{ km s}^{-1}$ and a covering factor $f_c = 0.001$ per clump, the number of small clumps in the beam will be $n_c \approx 4 \times 10^3$. If we further assume a radius of 100 AU for the clumps (approximately corresponding to 0.1% of the area of a background source with a diameter of 6000 AU) and a density $n_{\text{H}_2} = 10^4 \text{ cm}^{-3}$, Eq. (10) gives a column density $N(\text{H}_2) \approx 8 \times 10^{22} \text{ cm}^{-2}$. The corresponding CO column density, derived solely from the observed opacity and assuming $f_c \approx 1$, would in this case be $3 \times 10^{15} \text{ cm}^{-2}$, which translates to a H_2 column density of $6 \times 10^{19} \text{ cm}^{-2}$. This simple exercise shows that *the column density can be underestimated by three orders of magnitude if the molecular ISM is made up of small dense clumps rather than a diffuse medium.*

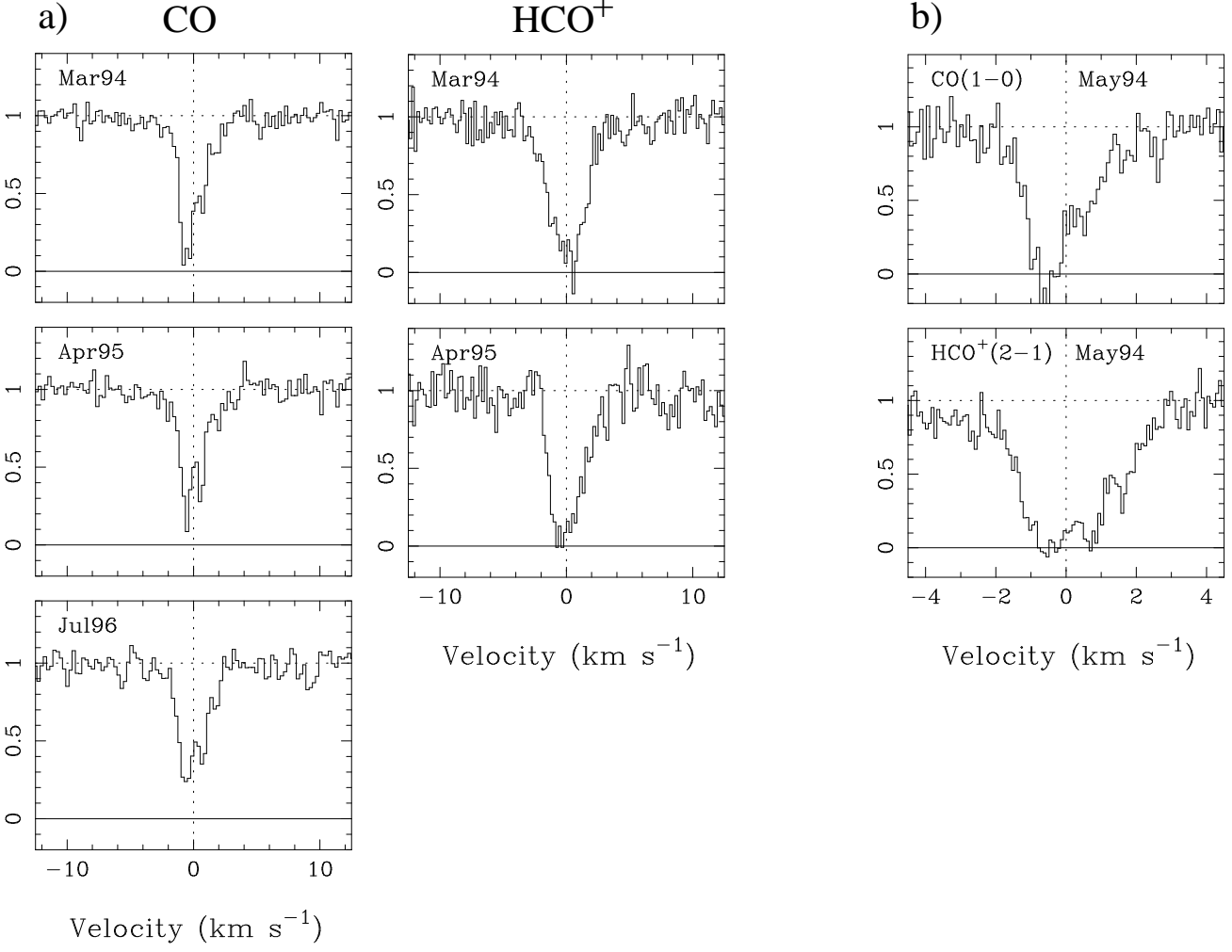


Fig. 8. **a)** Normalized spectra of the $J=0 \rightarrow 1$ transition of CO obtained in March 1994, April 1995 and July 1996 and the $J=1 \rightarrow 2$ transition of HCO^+ obtained in March 1994 and April 1995. The velocity resolution is 0.25 km s^{-1} for the CO spectra and 0.20 km s^{-1} for the HCO^+ spectra. **b)** Normalized spectra of the $J=0 \rightarrow 1$ transition of CO and the $J=1 \rightarrow 2$ transition of HCO^+ both obtained in May 1994 with a velocity resolution of 0.095 km s^{-1} and 0.082 km s^{-1} , respectively. The velocity scale is heliocentric and the dashed line corresponds to zero velocity for a redshift $z = 0.24671$.

4.5. Time variability

In Fig. 8 we show the $\text{CO}(0 \rightarrow 1)$ and $\text{HCO}^+(1 \rightarrow 2)$ absorption lines for different epochs, spanning 2 years for CO and 1 year for HCO^+ . In Fig. 8b we show the CO and HCO^+ line at higher velocity resolution. While there are no apparent changes within the noise in the HCO^+ spectra between March 1994 and April 1995, the CO line appears to have changed. A closer inspection of the CO absorption reveals that it is the deepest absorption component that has changed while the second deepest component remains more or less constant. In order to quantify possible variations we fit 3 Gaussian components to the CO spectra from all observed epochs. The components are illustrated in Fig. 9 and the Gaussian parameters are listed in Table 4, together with the integrated opacities derived from the

Gaussian fits. The data from February 1994 are of poor quality, as seen from the high χ^2 value of the Gaussian fit, and will not be used in the analysis. The integrated opacities show that while the second deepest absorption component (no. 2 in Table 4) does not show any significant variation, the main component (no. 1) changes by a factor of >2 in velocity integrated opacity. The third component is much weaker and less clearly defined. The Gaussian fit for this component is therefore more questionable than for components 1 & 2, which show consistent center velocities and half widths for the different epochs.

How certain are these results? Changes in the integrated opacity could be mimicked by an incorrectly derived continuum level, if this is caused by calibration errors. However, pure pointing uncertainties would not affect the *ratio* of the components. It is difficult to quan-

Table 4. Gaussfits to the CO(0→1) line.

| Date | $T_c^a)$ | Comp. | $T_{\text{abs}}^b)$ | $V_c^c)$ | $\Delta V_{1/2}^d)$ | χ^2 | $[\int \tau_\nu dV]_i^e)$ | $[\int \tau_\nu dV]_{\text{tot}}^f)$ | $R^g)$ |
|-------|----------|-------|---------------------|--------------------|---------------------|----------|---------------------------|--------------------------------------|---------------------|
| | | | | km s ⁻¹ | km s ⁻¹ | | km s ⁻¹ | km s ⁻¹ | |
| Feb94 | 0.46 | 1 | 0.91 | -0.7 | 0.9 | 4.87 | 2.6 | 3.2 ± 0.2 | — |
| | | 2 | 0.38 | +0.5 | 1.9 | | 1.5 | | |
| | | 3 | 0.07 | +1.1 | 7.4 | | 0.9 | | |
| Mar94 | 0.68 | 1 | 0.97 | -0.5 | 1.3 | 0.44 | 2.8 | 3.80 ± 0.05 | $5.6^{+0.8}_{-0.8}$ |
| | | 2 | 0.56 | +0.7 | 0.6 | | 0.48 | | |
| | | 3 | 0.25 | +1.8 | 1.1 | | 0.31 | | |
| May94 | 1.00 | 1 | 1.10 | -0.6 | 1.2 | 0.83 | >3.3 | 4.07 ± 0.07 | $> 7.0^{+0}_{-0.8}$ |
| | | 2 | 0.47 | +0.6 | 0.8 | | 0.47 | | |
| | | 3 | 0.15 | +1.6 | 1.9 | | 0.32 | | |
| Apr95 | 0.48 | 1 | 0.83 | -0.6 | 1.1 | 0.31 | 1.6 | 3.00 ± 0.06 | $3.3^{+0.3}_{-0.1}$ |
| | | 2 | 0.62 | +0.6 | 0.6 | | 0.49 | | |
| | | 3 | 0.20 | +1.7 | 1.9 | | 0.42 | | |
| Jul96 | 0.31 | 1 | 0.77 | -0.6 | 1.5 | 0.60 | 1.9 | 2.98 ± 0.06 | $3.1^{+0.2}_{-0.1}$ |
| | | 2 | 0.56 | +0.8 | 0.8 | | 0.61 | | |
| | | 3 | 0.31 | +1.8 | 0.6 | | 0.63 | | |

a) Continuum flux normalized to the flux at May 1994.

b) The depth of the absorption line from the normalized continuum level.

c) The center velocity of the Gauss component.

d) Full width at half intensity.

e) Integrated opacity of individual components derived from the Gaussian fits.

f) Total integrated opacities from the observed profiles.

g) Ratio of integrated opacities of component 1 and 2. Errors correspond to $\pm 10\%$ variation of the continuum level.**Table 3.** Column densities

| Molecule | $\gamma^a)$ | $T_{\text{cold,diffuse}}$ | $T_{\text{warm,dense}}$ | N |
|------------------|-------------|---------------------------|-------------------------|----------------------|
| | | K | K | cm ⁻² |
| CO | 0.22 | 3.9 | 18.0 | 2.0×10^{16} |
| HCN | 0.05 | 3.4 | 27.0 | 2.0×10^{13} |
| HNC | 0.05 | 3.4 | 27.0 | 1.0×10^{13} |
| HCO ⁺ | 0.22 | 3.9 | 18.0 | 4.5×10^{13} |

a) The fraction of the column density in the cold gas component.

tify the errors associated with multicomponent Gaussian fits to absorption spectra. The errors associated with the total velocity integrated opacity are small (see Table 4). Hence, as long as the Gaussian fit is good, the error in the integrated opacity for the separate components is small ($\lesssim 5\%$). The dominating uncertainty is associated with

errors in the continuum level caused by an unstable atmosphere. This can be minimized by taking the ratio of integrated opacities for the first and second component (last column in Table 4), but due to the non-linear relation between the depth of the absorption profile and the opacity a small uncertainty remains. The continuum level is derived using $\gtrsim 10$ individual spectra plus a number of special continuum observations. Each of these has a typical uncertainty of $\pm 15\%$. The final uncertainty associated with the continuum level from the average of these individual measurement is approximately $\pm 5\%$. In order to quantify the uncertainty of the integrated opacities introduced by errors in the continuum level, we have done the analysis (Gaussian fits and derivation of opacities) with a continuum level varying $\pm 10\%$ around the observed value. This is a conservative estimate and nevertheless shows that the ratio of the integrated opacity of the first and second absorption components has varied from $\gtrsim 7$ in May 1994 to ~ 3 in 1995 and 1996. The ratio of R between May 1994 and July 1996, including the assumed errors of $\pm 10\%$ in the continuum level, is 2.3 ± 0.3 .

The fact that we do not see any clear changes in the HCO⁺ line is not contradictory. The opacity of the HCO⁺ absorption is higher than that of CO, making it less sensitive to changes in the continuum level. Moreover, the abundance ratio HCO⁺/CO is higher in low density envi-

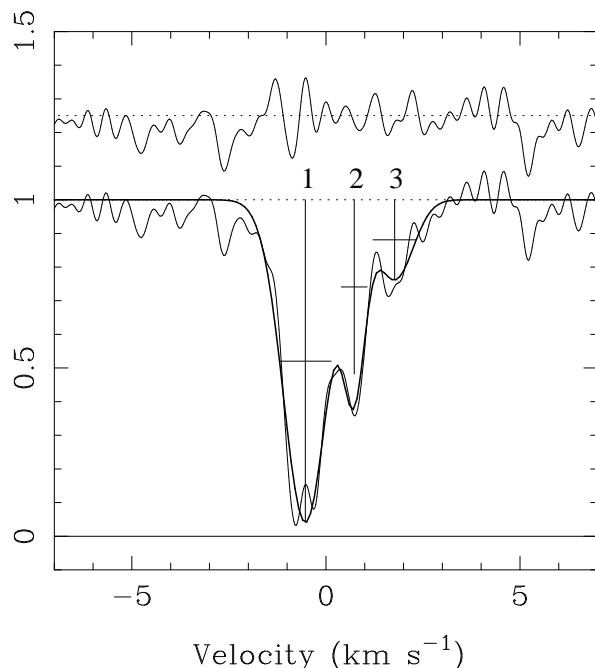


Fig. 9. Three component Gaussian fitted to the CO(0→1) absorption for the spectrum obtained in March 1994. The residual is shown above the spectrum. The parameters of the Gauss fit is given in Table 3. The numbers correspond to the components as listed in Table 3.

ronments than at high densities (cf. Lucas & Liszt 1996), with the HCO⁺ molecule existing in low density regions where CO self-shielding is not taking place.

5. Discussion

5.1. Small scale structure in the molecular gas

In the Milky Way, several lines of evidence suggest that the molecular ISM is clumpy on all scales from 20 AU to 100 pc and characterized by a fractal structure (cf. Falgarone et al. 1992). Time variations in Galactic H₂CO absorption towards extragalactic point sources (Marscher et al 1993) even suggest structures in the molecular ISM on scales of 10 AU. Through numerical simulations Marscher & Stone (1994) were able to derive constraints on the fractal structure of molecular clouds from the time variability detections. The mean number of small clumps along the line of sight should be larger than previously thought, i.e. the size spectrum of clumps should be a steeper power-law, constraining the fractal dimension. Detailed multi-level studies of CO and CS near the edge of a nearby molecular cloud complex have revealed that the molecular ISM is confined to small structures (down to 35 AU) which are dense ($n_{\text{H}_2} \sim 10^4 \text{ cm}^{-2}$), cold ($T_K \sim 10 - 15 \text{ K}$) (Falgarone & Phillips 1996) and characterized by a fractal structure (Falgarone et al. 1992). In fact, Falgarone

& Phillips (1996) find no evidence for a pervasive diffuse molecular ISM, although this could be a peculiarity for the specific region studied. Although emission studies are not sensitive to the pervasive diffuse medium, the absorption studies of Lucas & Liszt (1996) and Liszt & Lucas (1996) show a higher rate of molecular absorption in the Galaxy than was originally expected, and precisely detect the low-opacity, large-covering factor medium.

Small scale structures are also present in the atomic ISM. Multi-epoch observations of 21 cm absorption against high velocity pulsars have detected opacity variations of the ISM on a range of scales from 5 AU to 100 AU (Frail et al. 1994). VLBI observations at 21 cm in front of 3C radio sources have shown clumps on a scale of 25 AU (Diamond et al. 1989, Davis et al. 1996). In the case of 21 cm absorption against pulsars, where small-scale opacity structures are detected towards *all* line of sights, the mean opacities are between 0.1 and 2.5, corresponding to N(HI) as low as $10^{19} - 10^{20} \text{ cm}^{-2}$ (Frail et al. 1994). The opacity variations detected are quite high (half of them have $\delta\tau > 0.1$, Frail et al. 1994), so they cannot be accounted for by mild density fluctuations. Clumps with density larger than $10^5 - 10^6 \text{ cm}^{-3}$ are implied (Moore & Marscher 1995). These clumps could represent 10–20% of the total column density. Small dense clumps in the atomic gas has also been inferred in high redshift radio galaxies (van Ojik et al. 1997), where absorption within the Ly- α emission regions suggest the presence of neutral atomic clumps of size $\sim 0.03 \text{ pc}$.

Is the molecular gas along the line-of-sight towards PKS1413+135 similar to that of our Milky Way concerning small scale structure? Combining our molecular absorption line data with X-ray data gives three arguments which suggest the presence of a molecular ISM consisting of small dense clumps embedded in a more diffuse medium:

- The excitation temperatures for three transitions of HCO⁺ are consistent with a multicomponent molecular gas. If two or more components coexist along the line-of-sight, the assumption of a single gas component underestimates the true column density.
- The total column density averaged over the extent of the background source and along the line-of-sight (atomic and molecular) is much lower than that derived from the deficiency of low energy X-ray photons. Since the covering factor of gas appears to be high, this implies that we indeed underestimate the total column of gas.
- Possible time variations in the depth of the molecular absorption lines indirectly suggests the presence of small scale structure.

The first item has been presented in Sect. 4.3 and 4.4. Below we discuss the second and third item in more detail.

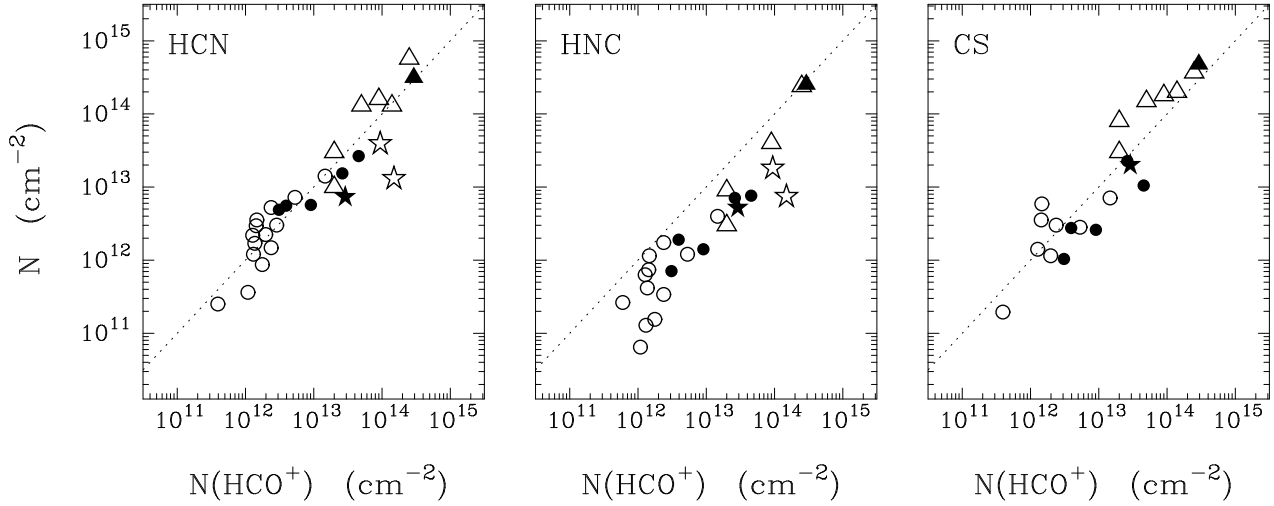


Fig. 10. Column density of HCO^+ plotted versus column densities of HCN, HNC and CS. The open circles represent Galactic diffuse clouds (Lucas & Liszt 1994, 1996), filled circles represent data from Cen A (Wiklind & Combes 1997) and open triangles represent absorption data towards SgrB2 (Greaves & Nyman 1996). The filled star represents our absorption data for PKS1413+135, open stars from B3 1504+377 at $z=0.673$ (Wiklind & Combes 1996b) and the filled triangle PKS1830-210 at $z=0.886$ (Wiklind & Combes 1996a). The dashed line is a one-to-one correspondence between the column densities and is not a fit to the data.

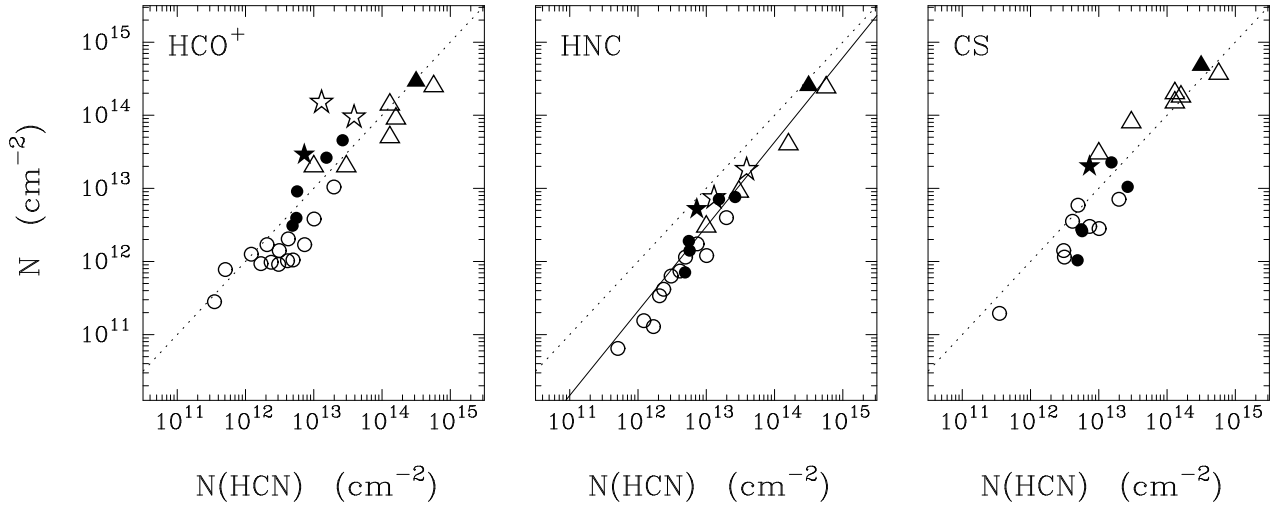


Fig. 11. Column density of HCN plotted versus column densities of HCO^+ , HNC and CS. Designations are as in Fig. 10. The full-drawn line in $N(\text{HCN})$ vs. $N(\text{HNC})$ is a linear fit to the data, showing how the HCN/HNC ratio increases with decreasing HCN column density (see text for details).

5.1.1. The extinction towards PKS1413+135

The minimum column density of molecular hydrogen towards PKS1413+135, inferred directly from the $\text{CO}(0\rightarrow1)$ absorption, is $4 \times 10^{20} \text{ cm}^{-2}$ (Sect. 4.1). Together with the estimated HI column density of $1 \times 10^{21} \text{ cm}^{-2}$ (where we have assumed a covering factor of unity and a spin temperature of 100 K), the total column of hydrogen, $N(\text{H}) =$

$2N(\text{H}_2) + N(\text{HI})$, is $\sim 2 \times 10^{21} \text{ cm}^{-2}$. This is more than 10 times lower than the column inferred from the deficiency of low energy X-ray photons which indicates $A_v > 30 \text{ mag}$ (Stocke et al. 1992). Is this discrepancy caused by an imprecise X-ray measurement, by the particular distribution of the obscuring gas relative to the radio core, or by an underestimate of the molecular and/or atomic column den-

sity? McHardy et al. (1994) analyzed ROSAT observations of PKS1413+135 in the 0.4–2.4 keV range. Although they did not obtain enough data for a complete spectrum, the very low flux of low-energy X-ray photons measured by ROSAT is consistent with the deficiency observed by the Einstein satellite (Stocke et al. 1992). It is thus not likely that the X-ray results are erroneous. Also, the absence of any lines from both the narrow- and broad emission line regions, even when viewed in the near-IR (McHardy et al. 1994; Stocke et al. 1992; Perlman et al. 1996), indicates that the extinction is very high. An obscuring dusty torus around the AGN can cause a large extinction. In Cyg A, for instance, the optical extinction, originating in a torus near the center, is estimated to be ~ 170 mag, or $N(\text{H}) = 3.75 \times 10^{23} \text{ cm}^{-2}$ (Ueno et al. 1994). Although 21 cm HI absorption is detected (Conway & Blanco 1995), no molecular absorption is seen despite this high column density (Drinkwater et al. 1995). The non-detection of molecular absorption could be due to either a lack of molecular gas as such, or that the gas is dense enough to render the excitation temperature very high, depopulating the lower rotational levels of existing molecules, or that the molecular rotational levels are radiatively coupled with the ambient radiation field (e.g. Maloney et al. 1994). The presence of a dense torus in PKS1413+135, similar to Cyg A, is, however, not likely in view of the absence of a near-infrared excess emission, caused by dust grains heated to high temperatures. This implies that the column density of the molecular gas in PKS1413+135, which should be situated at a relatively large distance from the AGN in order to explain the lack of near-infrared emission, and to be compatible with the very narrow line-width, is severely underestimated, strongly suggesting the presence of a dense clumpy medium as emphasized in previous sections.

5.1.2. Time variability

Changes in the absorption lines towards background continuum sources can be caused either by motions of small scale structure in the absorbing gas across the angular extent of the radio core, or by spatial changes in the radio core itself. Such variations can give important information about both the size of the radio core and of the scale spectrum of the molecular interstellar medium.

The radio source PKS1413+135 consists of a compact radio core and several emission components on a parsec-scale, while no radio emission is seen at scales of kiloparsecs (Perlman et al. 1994, 1996). The parsec-scale components all have a steep-spectrum and do not contribute to the flux at millimeter wavelengths. The core has a spectral index $\alpha = +1.7$ between $\lambda 18\text{cm}$ and $\lambda 3\text{cm}$ (Perlman et al. 1996). The core remains unresolved at an angular resolution of 2.3 mas, corresponding to $\sim 7\text{pc}$. It is, however, likely to be significantly smaller. Perlman et al. (1996) derive a lower limit to the size of the core from the variability time-scale of $\sim 10\ \mu\text{arcsec}$, corresponding to $\sim 0.03\text{pc}$.

The galaxy associated with PKS1413+135 is seen edge-on (McHardy et al. 1994) and we can therefore expect that the transverse velocity is equal to the rotational velocity. The latter is unknown but likely to be $\sim 250\text{ km s}^{-1}$. This corresponds to a transverse shift of 50 AU yr^{-1} . The time scale for a significant change of the gas properties due to a shift of the obscuring molecular gas is therefore at least 100 years, possibly much longer. The only possibility to explain much shorter variations is the existence of high velocity ($\gtrsim 25\,000\text{ km s}^{-1}$) shocks propagating outwards from the radio core.

In Table 4 we also give the continuum flux relative to that of May 1994 (which was the highest during the extent of these observations). The deepest absorption (largest ratio of the first and second component) occurs when the continuum flux is at maximum, suggesting that the changes are due to structural changes in the background radio source rather than transverse motion of small scale structure in the molecular gas. Knowing the extent of the changes of the radio core during an outburst would give us a limit to the size of the molecular gas structures. Future mm-VLBI observations may provide such data. Also, the change in component 1 is likely to be recurrent with the next outburst, if this takes place in the same region of the radio core.

5.2. Molecular cloud properties

The inferences to be made from the analysis of multicomponent molecular gas along the line of sight to PKS1413+135 (Sect. 4.3 & 4.4) is that it is not possible to derive a correct column density without knowledge about the structure of the molecular ISM. However, if we can assume homogeneity for the physical and chemical conditions over the extent of the background source and along the line of sight, we can quite confidently derive abundance ratios³. Furthermore, assuming similarities between the structure of the molecular ISM in PKS1413+135 and the Milky Way, we can compare our column densities with those derived for our Galaxy through similar observing methods (i.e. absorption line measurements). These assumptions are justified by the small amount of molecular gas that actually contributes to the observed absorption. The angular extent of the background continuum source is of the order $10\text{--}30\ \mu\text{arcsec}$, as implied by time variability (Perlman et al. 1996) and by inferences from mm-wave VLBI of a similar radio source (Lerner et al. 1993). The amount of molecular hydrogen probed by the line of sight to PKS1413+135 is thus only $(0.5 - 2) \times 10^{-2} M_{\odot}$, where we have used $N(\text{H}_2) = 4 \times 10^{20} \text{ cm}^{-2}$ (cf. Sect. 4.1). The size-linewidth relation found for molecular clouds in the Milky Way (Larson 1981; Solomon et al. 1987) implies that the molecular gas is extended $\sim 1\text{pc}$ along the line of sight. Assuming that most of the mass is contained in

³ Abundance is used in synonym with column density while discussing column density *ratios*.

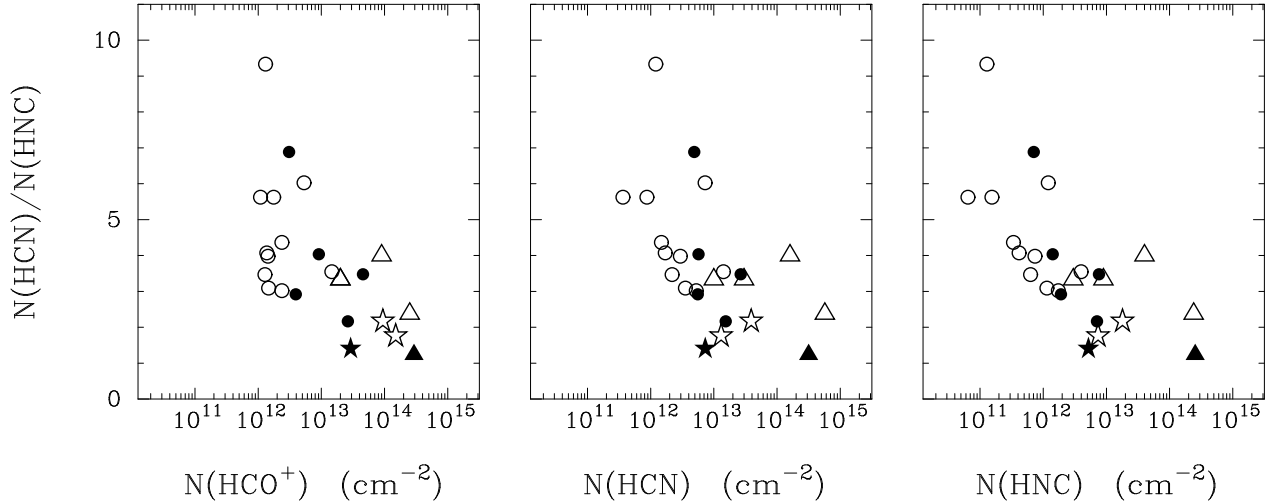


Fig. 12. The HCN/HNC ratio versus the column density of HCO^+ , HCN and HNC. The trend of decreasing HCN/HNC abundance ratio with increasing column density of HCN indicated in Fig. 11 is clearly visible. Designations are as in Fig. 10.

small clumps with $n(\text{H}_2) = 10^4 \text{ cm}^{-3}$ (Sect. 4.4), the total H_2 mass is $f_V(0.4 - 4) \text{ M}_\odot$, where f_V is the volume filling factor of the dense clumps. f_V is likely to be $\ll 1$. In either case we are dealing with a very small portion of the molecular ISM in the galaxy at $z=0.247$. In Table 5 we present abundance ratios for PKS1413+135. The column densities are taken from Table 2. The upper and lower limits represents 1σ limits. Below we discuss in some more detail various results that can be derived from these abundance ratios.

5.2.1. Molecular oxygen O_2

One of the more interesting questions in interstellar chemistry is the abundance of O_2 , which is supposed to bind most of the free oxygen atoms and to be one of the most important coolants (e.g. Goldsmith & Langer 1978). This molecule has yet to be observed in the ISM. The redshift of PKS1413+135 shifts the main $\text{N}(\text{J})=1_0 \rightarrow 1_1$ line of O_2 , which is usually not observable from the ground, to an easily accessible window (95.25 GHz). However, the rather low average opacity means that our limit to $\text{O}_2/\text{CO} < 0.3 \pm 0.09$ is 20 times higher than the upper limit derived towards B0218+357 at $z=0.68$ (Combes & Wiklind 1995). Nevertheless, this limit is of interest since it concerns the ground state and thus is sensitive to excitationally very cold gas. The transitions observed in B0218+357 were the $\text{N}(\text{J})=1_2 \rightarrow 3_2$ and the $\text{N}(\text{J})=1_1 \rightarrow 3_2$ lines. The 1_1 level can not be directly populated from the ground state through collisions, but has to be populated through collisional excitation from $\text{N}(\text{J})=1_0$ to 1_2 and 3_2 (Bergman 1995). The latter energy level corresponds to a temperature $\sim 23 \text{ K}$. Radiative transitions from the ground state to the $\text{N}(\text{J})=1_1$ level is allowed and probed by the obser-

vations presented here. This transition has now also been observed in B0218+357, giving an improved upper limit to the O_2/CO ratio for this system (Combes & Wiklind 1997).

Table 5. Abundance ratios

| | | | | |
|---|------|-------|------|-----------|
| $\frac{\text{O}_2}{\text{CO}}$ | <0.3 | \pm | 0.1 | |
| $\frac{\text{O}_2}{\text{HCN}}$ | <0.9 | \pm | 0.3 | 10^3 |
| $\frac{^{12}\text{CO}}{^{13}\text{CO}}$ | >74 | \pm | 53 | |
| $\frac{\text{H}^{12}\text{CO}^+}{\text{H}^{13}\text{CO}^+}$ | >111 | \pm | 6 | |
| $\frac{\text{HCN}}{\text{CS}}$ | >1.1 | \pm | 0.3 | |
| $\frac{\text{HCN}}{\text{H}_2\text{CO}}$ | >1.5 | \pm | 0.6 | |
| $\frac{\text{HCN}}{\text{N}_2\text{H}^+}$ | >10 | \pm | 3 | |
| $\frac{\text{HCO}^+}{\text{CO}}$ | 1.3 | \pm | 0.4 | 10^{-3} |
| $\frac{\text{HCN}}{\text{HCO}^+}$ | 0.25 | \pm | 0.07 | |
| $\frac{\text{HCN}}{\text{CN}}$ | 0.4 | \pm | 0.2 | |
| $\frac{\text{HCN}}{\text{HNC}}$ | 1.4 | \pm | 1.0 | |

5.2.2. Isotopic ratios

The isotopic abundance ratios for CO and HCO^+ presented in Table 5 suggests relatively low abundances of the ^{13}C isotopic variants. The large formal error for $^{12}\text{CO}/^{13}\text{CO}$ comes from the assumed range of excitation temperatures (cf. Table 2). Since the abundance ratio is largely independent of T_{ex} , the true uncertainty of this ratio is much smaller. In the ISM of the Milky Way the $^{12}\text{C}/^{13}\text{C}$ isotope ratio varies from ~ 20 in the Galactic center region to ~ 70 in the local ISM (Wilson & Matteucci 1992). The correlation between the $^{12}\text{C}/^{13}\text{C}$ ratio and that of the substituted isotopic molecules depends on chemical fractionation (enhancing the isotopic variants) and selective photoinization (decreasing the isotopic species due to less self-shielding). In Galactic molecular clouds as well as in nearby galaxies, the final result is an increase in the $^{12}\text{CO}/^{13}\text{CO}$ ratio (and likewise for HCO^+) compared to the actual $^{12}\text{C}/^{13}\text{C}$ ratio. The high lower limits found in PKS1413+135 therefore suggests a low ^{13}C abundance relative to ^{12}C .

Whereas ^{12}C is produced in both low and high mass stars, as a primary product of hydrostatic burning, ^{13}C is only produced through incomplete proton burning in the red giant stage of low and intermediate mass stars (e.g. Wilson & Matteucci and references therein). A low ^{13}C abundance may therefore indicate a young chemistry, where the low and intermediate mass stars have not yet had time to reach the red giant stage. ^{14}N is produced and ejected into the ISM in much the same way as ^{13}C . The high lower limit $\text{HCO}^+/\text{N}_2\text{H}^+ > 41$ found in PKS1413+135 is therefore in agreement with the interpretation that the low and intermediate mass stars have not yet reached their red giant stage. In PKS1830-211 at $z=0.89$, we found a $\text{HCO}^+/\text{N}_2\text{H}^+$ ratio of ~ 1.4 (Wiklind & Combes 1996a). In this molecular absorption line system we also detect several ^{13}C isotopic species. Although it is not entirely clear whether this is due to an extremely high opacity, PKS1830-211 seems to be more chemically evolved than PKS1413+135, despite the much higher redshift.

5.2.3. Dark cloud chemistry

The equilibrium abundances in dark clouds (i.e. molecular gas where the main ionization source is cosmic rays) can be divided into a High and Low Ionization Phase (HIP and LIP) (Flower et al. 1994; Le Bourlot et al. 1995; Gerin et al. 1997). The LIP is characterized by a chemistry driven by ion-molecule reactions where proton transfer involving H_3^+ plays a major role. The C/CO ratio is low and most of the gas phase carbon is locked up in CO. This phase has a high abundance of O_2 and molecular ions such as HCO^+ and N_2H^+ . Other carbon bearing molecules, such as CN, have low abundances. The HIP has a chemistry driven by charge transfer reactions involving H^+ and is characterized by a large C/CO ratio. This leads to low abundances of

O_2 and molecular ions. Abundances of HCN and HNC are only marginally affected by the ionization state of the gas. The abundance ratios presented in Table 5 mainly uses HCN as a ‘reference’.

Are our abundance ratios for PKS1413+135 consistent with either of these two phases for dark cloud chemistry? Comparing our abundance ratios with the model results of Le Bourlot et al. (1995) we find that our O_2/CO ratio does not constrain the ionization state of the gas, although our limit is of the same order as the expected O_2/CO ratio for the low ionization phase. Our limit to the O_2/HCN ratio is only compatible with a high ionization phase, while our abundance ratios for HCN/CO, HCN/HNC and the lower limit to HCN/CS only are compatible with a low ionization phase. Hence, the molecular absorption line data for PKS1413+135 does not present a clear-cut case for either of the two ionization phases. Also, the HCO^+/CO ratio is too large, by more than an order of magnitude, to be compatible with either the high or low ionization phase. However, as discussed by Hogerheijde et al. (1995), turbulence might influence the chemistry, producing enhanced amounts of HCO^+ . If this is the case for the high abundance of HCO^+ this would indicate a diffuse gas, since the proposed formation pathway is quenched at $n(\text{H}_2) \gtrsim 10^3 \text{ cm}^{-3}$. Dark cloud chemistry shows bi-stability and can switch from one phase to the other on a short time scale (Le Bourlot et al. 1992, 1995), making it possible to have a mixture of ionization phases over small spatial scales. Improved limits on the O_2 and CS abundances may enable us to put limits to the amount of gas along the line of sight to PKS1413+135 that can exist in HIP and LIP states.

5.2.4. Comparison of column densities

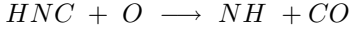
In Fig 10 we plot the column density of HCO^+ versus the column densities of HCN, HNC and CS. The plot contains data from Galactic absorption measurements in low density gas (Lucas & Liszt 1993, 1994, 1996) and in higher density gas seen towards Sgr B2 (Greaves & Nyman 1996), as well as our recent results from absorption line measurements towards Cen A (Wiklind & Combes 1997). In addition, we include results from two additional high- z molecular absorption line systems 1504+377 at $z=0.67$ (Wiklind & Combes 1996b) and PKS1830-211 at $z=0.89$ (Wiklind & Combes 1996a). The dotted line is a one-to-one correspondence between the column densities and not a fit to the data. In Fig. 11 we plot the column densities of HNC and CS versus HCN in the same way as in Fig. 10. Despite the presence of a considerable scatter, the most striking impression from the figures is the remarkable correlation, over more than 3 orders of magnitude, in column density. This suggests that the chemistry is similar for these simple molecules in environments characterized by very different column densities. The high- z systems do not show any peculiarities compared to the local values, suggesting that the

molecular ISM offers similar conditions for star formation at earlier epochs as it does in the present one.

The only trend in abundance ratios is found between HCN and HNC (Fig. 11), where the abundance of HNC seems to decrease relative to HCN with decreasing HCN abundance. The solid line is a least-square fit to the HNC vs. HCN abundances:

$$N(\text{HNC}) = 2.3 \times 10^{-3} [N(\text{HCN})]^{1.16} . \quad (10)$$

In Fig. 12 we plot the HCN/HNC abundance ratio as a function of the HCO^+ , HCN and HNC column densities. The HCN/HNC ratio decreases with increasing column density in all three cases. Isomers like HCN and HNC have similar chemistry, only differing in a few key reactions which determine the abundance ratio. Through chemical modelling of the HCN and HNC abundances Schilke et al. (1992) found that the HCN/HNC ratio increases with increasing kinetic temperature (cf. Irvine et al. 1987) as well as with increasing molecular hydrogen density, n_{H_2} . The reason for this is primarily the key reactions



which are effective at relatively high temperatures and preferentially destroy HNC relative to HCN. A large column density does not necessarily imply a large volume density of H_2 and, since the abundance of HCN is less dependent on T_k for low H_2 abundances (Schilke et al. 1992), the correlations between the HCN/HNC and column densities seen in Fig. 12 is likely to be a temperature effect, affecting primarily the HNC abundance. The lowest column densities being associated with the kinetically warmest gas. However, the dependence of the HCN/HNC abundance ratio on *both* temperature and density makes it less valuable as a temperature probe than previously thought.

The high- z systems all tend to have HCN/HNC ratios ~ 2 , among the lowest of the line-of-sights presented in Figs. 10–12. It is unclear whether this is a selection bias towards both kinetically and excitationally cold gas, or an effect of low metallicity, making the HNC depletion reactions less effective.

5.3. Invariance of physical constants

A potential diagnostic application of molecular absorption lines at high redshift is to check the invariance of fundamental physical parameters. (cf. Thompson 1975). The energy difference between two adjacent rotational levels in a molecule consisting of two atoms is proportional to $(\mu r^2)^{-1}$, where r is the bond length and μ is the reduced mass of the atoms. A vibrational transition of the same molecule has, to a first order approximation, a $\mu^{1/2}$ dependence on the reduced mass. Comparison of

Table 6. Redshifts and variations of molecular mass

| Transition | z_a | $\left[\frac{\Delta z}{(1+z)}\right]^a$ |
|--|--|--|
| PKS1413+135 | | |
| HI | $0.24671 \pm 1 \times 10^{-5}$ | — |
| CO(0→1) | $0.2467091 \pm 3 \times 10^{-7}$ | $(+0.7 \pm 8.0) \times 10^{-6}$ |
| HCN(1→2) | $0.2467112 \pm 1 \times 10^{-6}$ | $(-0.9 \pm 8.1) \times 10^{-6}$ |
| HNC(2→3) | $0.2467105 \pm 3 \times 10^{-7}$ | $(-0.4 \pm 8.0) \times 10^{-6}$ |
| $\text{HCO}^+(1\rightarrow 2)$ | $0.2467102 \pm 3 \times 10^{-7}$ | $(-0.2 \pm 8.0) \times 10^{-6}$ |
| $\text{HCO}^+(2\rightarrow 3)$ | $0.2467097 \pm 3 \times 10^{-7}$ | $(-0.2 \pm 8.0) \times 10^{-6}$ |
| HNC(1→2) | $0.2467114 \pm 3 \times 10^{-7}$ | $(-1.1 \pm 8.0) \times 10^{-6}$ |
| B0218+357 | | |
| HI | $0.68466 \pm 4 \times 10^{-5}$ | — |
| $^{13}\text{CO}(1\rightarrow 2)$ | $0.684693 \pm 1 \times 10^{-6}$ | $(+2.0 \pm 2.4) \times 10^{-5}$ |
| B3 1504+377 | | |
| HI | $0.67324 \pm 1 \times 10^{-5}$ $0.67343 \pm 1 \times 10^{-5}$ | — — |
| $\text{HCO}^+(1\rightarrow 2)$ | $0.673184 \pm 1 \times 10^{-6}$ $0.673327 \pm 1 \times 10^{-6}$ | $(-3.4 \pm 0.6) \times 10^{-5}$ $(-6.2 \pm 0.6) \times 10^{-5}$ |
| PKS1830 | | |
| HI | — | — |
| $\text{HCO}^+(1\rightarrow 2)$ | $0.8858261 \pm 3 \times 10^{-7}$ | |
| $\text{H}^{13}\text{CO}^+(1\rightarrow 2)$ | $0.8858647 \pm 6 \times 10^{-7}$ | |
| $\text{HCO}^+(2\rightarrow 3)$ | $0.8858298 \pm 3 \times 10^{-7}$ | |
| $\text{N}_2\text{H}^+(1\rightarrow 2)$ | $0.8858262 \pm 4 \times 10^{-7}$ | |
| $\text{H}_2\text{CO}(1_{10} \rightarrow 2_{11})$ | $0.8858263 \pm 4 \times 10^{-7}$ | |
| CS(2→3) | $0.8858295 \pm 3 \times 10^{-7}$ | |

a) $\Delta z/(1+z) = (z_{\text{HI}} - z_{\text{mol}})/(1+z_{\text{HI}})$

HI references: PKS1413+135 (Carilli et al. 1992), B0218+357 (Carilli et al. 1993), B3 1504+377 (Carilli et al. 1996).

Molecular line references: PKS1413+135 (this paper), B0218+357 (Combes & Wiklind 1995), B3 1507+377 (Wiklind & Combes 1996b), PKS1830–211 (Wiklind & Combes 1996a, 1997).

a vibrational-rotational spectrum from an earlier epoch with a present one can therefore be used to set limits on the changes of the proton and neutron masses. This has been done for molecular hydrogen seen in absorption in a damped Lyman- α system at $z=2.81$ (Foltz et al. 1988, Varshalovich & Potekhin 1996), giving a limit of 2×10^{-4} to $\Delta m_p/m_p$. For pure rotational transitions one can compare the line frequencies (or similarly, the measured redshifts) with the frequencies of electronic transitions. This gives a measure of the invariance of the electron to proton mass. It is also possible to compare the 21 cm HI line with a molecular rotational line. The formers energy difference to first order depending on m_e^2 , again giving a measure

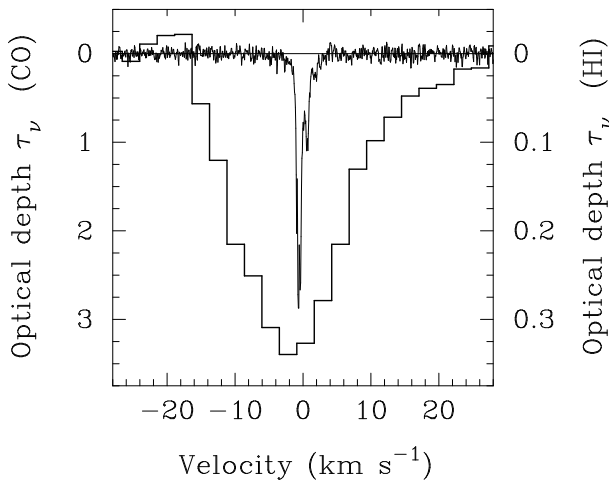


Fig. 13. A comparison of the CO(0→1) and 21 cm HI absorption towards PKS1413+135. In both cases the optical depth is plotted. Notice that Fig. 3 in Wiklind & Combes 1994 suffers from an erroneous velocity scale, causing the CO and HI lines to be separated by $\sim 11 \text{ km s}^{-1}$.

of the invariance of the m_e/m_p ratio (see also Tubbs & Wolfe 1980 for a comparison of the 21 cm line with optical resonance transitions).

In an Appendix we express the energy levels of molecular rotational lines in fundamental physical parameters. It is shown that for a differential measurement, i.e. measuring the redshifts of two different molecular species, $\Delta z/(1+z)$ is directly proportional to $\Delta\mu/\mu$. Strictly speaking, this is only valid when the molecule is approximated as a rigid rotator, but this is a good approximation for low lying J states. In Table 6 we list the observed redshifts of the molecular absorption lines in PKS1413+135, together with some lines from B 0218+357, B3 1504+377 and PKS1830-211. We also list the redshifts derived from 21 cm HI absorption when available. The redshifts have been obtained using Gaussian fits. We can compare both the redshifts derived for different molecules and the redshifts of the HI and molecular lines. If changes in the electron mass are negligible, the $\Delta z/(1+z)$ measures $\Delta\mu/\mu$, to first order, in both cases. The values given in Table 6 are the difference between the 21 cm HI and molecular redshifts. In Figure 13 we show the 21 cm HI absorption (Carilli et al. 1992) together with our CO(0→1) absorption towards PKS1413+135. It is quite clear that the HI spectra limit the accuracy with which Δz can be measured. Except for B3 1504+377, all the values in Table 6 are compatible with $\Delta z = 0$. For the 21 cm HI absorption obtained towards B3 1504+377 (Carilli et al. 1997), the discrepancy between HI and molecular velocities is of the order of 30 km s^{-1} , i.e. $\Delta z \approx 10^{-4}$, an order of magnitude larger than the HI accuracy. The HI result has been confirmed to an accuracy better than 1 km s^{-1} with

the Westerbork Synthesis Radio Telescope (Carilli et al 1997, preprint). Hence we reach here the basic limitation of the method, consisting of observing different atoms or molecules. It cannot be expected that all lines peak at the same velocity, since their local association is not perfect, and their excitation might be different. Supporting this, note that the molecular component in absorption in B3 1504+377 at $z = 0.67150$ has no HI counterpart.

To obtain more statistics, atomic and molecular absorptions in the Milky Way must be considered. Liszt & Lucas (1997) compared the absorption profiles of several different molecular lines with that of 21 cm HI and found that the velocity of the peak opacity often differs between the molecular and atomic lines. This shows that the absorptions do not arise in the same gas and any comparison is limited by the possible velocity difference of the two ISM components where the absorptions originates.

It is also possible to use different transitions from the same molecule to estimate $\Delta\mu/\mu$; While the rotational constant is proportional to μ^{-1} , the centrifugal distortion coefficient is proportional to μ^{-2} (Townes & Schawlow 1975). In the Appendix we show that we actually have a dependence on the invariance of the electron mass and the fine structure constant in this case. Comparing the $J=1\rightarrow 2$ and $J=2\rightarrow 3$ lines of HCO^+ in PKS1413+135 we get at the 1σ level: $\Delta z/(1+z) = (4.0 \pm 3.4) \times 10^{-7}$. Similarly for HCN: $\Delta z/(1+z) = (5.6 \pm 8.4) \times 10^{-7}$. Comparing CO(0→1) and $\text{HCO}^+(1\rightarrow 2)$ we get: $(-1.1 \pm 0.3) \times 10^{-6}$. This last result is marginally different from zero at a 3σ level. However, even when comparing molecular transitions one has to face the possibility that the lines do not come from the same location in phase space. HCO^+ , for instance, has been shown to exist in regions where the CO molecular is no longer self-shielded (Lucas & Liszt 1996), and its absorption profile can therefore be weighted with velocity components not seen in the CO line. A further complication is that HCO^+ is an ion and susceptible to magnetic fields present in the ISM. This can give it a drift velocity different from neutral molecular species. It is possible to have absorption lines dominated by different velocity components even when considering transitions from the same molecular species. This is due to the nonlinear dependence of the opacity to the excitation temperature (Sect. 4.2). Different transitions can therefore be weighted differently by gas along the line of sight.

To summarize, measurements of redshift differences between molecular absorption lines and 21 cm HI are likely to be dominated by velocity differences between the two gas components along the line of sight. This is a severe concern when comparing different molecular species and even different transitions of the same molecule. Taken at face value, the HI accuracy limits the nucleon mass variation to typically $\Delta\mu/\mu \lesssim 10^{-5}$ at a 3σ level. In one source (B3 1504+377) a discrepancy as large as 10^{-4} has been observed.

6. Summary

We present a multi-line study of an absorbing molecular cloud in the edge-on galaxy hosting the radio-source PKS1413+135, at $z=0.24671$. We have shown that the total column densities obtained are lower limits, since the absorption essentially traces the diffuse extended molecular gas, and is only weakly weighted towards the dense phase which provides most of the mass. The size of the absorbing structure along the line of sight must be of parsec scale, given its narrow total width. This situation is favorable to detect time variations in the absorption profile, if there exists knots in the radio source moving close to the velocity of light. Variations on time-scales of a month then correspond to structures of $> 10^3$ AU. We report possible time variation, affecting the relative ratio of two absorbing components, and therefore the shape of the profile. This is to a large extent independent of the continuum level and calibration uncertainties. Such time-variations are not surprising, in view of the small scale structure that has been detected in the ISM of the Milky Way.

Because of the high spectral precision of the millimeter techniques, it has been proposed that observation of molecules at high redshift could constrain variations of fundamental physical constants, such as the mass of the molecules. However, different molecules or different kind of lines (rotational, vibrational, etc..) should then be compared. Concerning the comparison between HI and molecular lines, it was shown that the HI accuracy limits the nucleon mass variation to $\Delta\mu/\mu \lesssim 10^{-5}$ at 3σ in many cases, but a discrepancy as large as 10^{-4} has been observed in one of the sources. Excitation problems in the not well-known multiphase structure of the medium prevents reaching conclusive results.

Acknowledgements. We are very grateful to the IRAM engineers and operators for the impressive work in tuning dizains of new frequencies during several observing runs and the generous allocation of observing time by IRAM. TW acknowledges support from NFR (the Swedish Natural Science Research Council) for this research.

References

Bergman P., 1995, ApJ 445, L167
 Bregman J.N., Lebofsky M.J., Aller M.F., et al., 1981, Nature 293, 714
 Briggs F., 1988, in QSO Absorption Lines, eds. J.C. Blades, D. Turnshek, C. Norman, Cambridge University Press, p. 275
 Carilli C.L., 1995, Journal of Astrophysics and Astronomy, Vol. 16 (Supplement), Proceedings of the Sixth IAU Asian-Pacific Regional Meeting, eds. V. Kapahi N. Dadhich, G. Swarup, and J. Narlikar, p. 163
 Carilli C.L., Menten K.M., Reid M.J., Rupen M.P., 1997, ApJ L89
 Carilli C.L., Rupen M.P., Yanny B., 1993, ApJ 412, L59
 Carilli C.L., Perlman E.S., Stocke J.T., 1992, ApJ 400, L13

Combes F., Wiklind T., 1996, in Cold Gas at High Redshift, eds. M.N. Bremer, P. van der Werf, H.J.A. Röttgering, C.L. Carilli, Kluwer Academic Pub., p. 215
 Combes F., Wiklind T., 1995, A&A 303, L61
 Conway J.E., Blanco P.R., 1995, ApJ 449, L131
 Davis, R.J., Diamond P.J., Goss W.M., 1996, MNRAS 283, 1105
 Diamond P.J., Goss W.M., Romney J.D. et al., 1989, ApJ 347, 302
 Drinkwater M., Combes F., Wiklind T., 1996, A&A 312, 771
 Falgarone E., Phillips T.G., 1996, ApJ 472, 191
 Falgarone E., Puget J.-L., Péroult M., 1992, A&A 257, 715
 Flower D.R., Le Boulrot J., Pineau des Forêts G., Roueff E., 1994, A&A 282, 225
 Foltz C.B., Chaffee F.H., Black J.H., 1988, ApJ 324, 267
 Frail D.A., Weisberg J.M., Cordes J.M., Mathers C., 1994, ApJ 436, 144
 Gerin M., Falgarone E., Joulain K., et al., 1997, A&A 318, 579
 Goldsmith P.F., Langer W.D., 1978, ApJ 222, 881
 Greaves J.S., Nyman L.-Å., 1996, A&A 305, 950
 Hogerheijde M.R., de Geus E.J., Spaans M., van Langevelde H., 1995, ApJ 441, L93
 Irvine W.M., Goldsmith P.F., Hjalmarson Å., 1987, in Interstellar Processes, eds. D.J. Hollenbach, H.A. Thronson, Reidel Publ. Co., p. 561
 Larson R.B., 1981, MNRAS 194, 809
 Le Boulrot J., Pineau des Forêts G., Roueff E., 1995, A&A 297, 251
 Le Boulrot J., Pineau des Forêts G., Roueff E., 1993, ApJ 416, L87
 Lerner M., Bååth L., Inoue M., et al., 1993, A&A 280, 117
 Liszt H., Lucas R., 1997 A&A, in press
 Liszt H., Lucas R., 1996 A&A, 314, 917
 Lovas F.J., 1992, J. Phys. Chem. Ref. Data 21, 181
 Lucas R., Liszt H., 1996, A&A 307, 237
 Lucas R., Liszt H., 1994, A&A 282, L5
 Lucas R., Liszt H., 1993, A&A 276, L33
 Maloney P.R., Begelman M.C., Rees M.J., 1994, ApJ 432, 606
 Marscher A.P., Moore E.M., Bania T.M., 1993, ApJ 419, L101
 Marscher A.P., Stone A.L., 1994, ApJ 433, 705
 McHardy I.M., Merrifield M.R., Abraham R.G., Crawford C.S., 1994, MNRAS 268, 681
 McHardy I.M., Abraham R.G., Crawford C.S., et al., 1991, MNRAS 249, 742
 Moore E.M., Marscher A.P., 1995, ApJ 452, 671
 Perlman E.S., Carilli C.L., Stocke J.T., Conway J., 1996, AJ 111, 1839
 Perlman E.S., Stocke J.T., Shaffer D.E., Carilli C.L., Ma C., 1994, ApJ 424, L69
 Schilke P., Walmsley C.M., Pineau des Forêts, et al., 1992, A&A 256, 595
 Solomon P.M., Rivolo A.R., Barrett J., Yahil A., 1987, ApJ 319, 730
 Stocke J.T., Wurtz R., Wang Q., Elston R., Jannuzi B.T., 1992, ApJ 400, L17
 Thompson R.I., 1975, Ap Letters 16, 3
 Townes C.H., Schawlow A.L., 1975, Microwave Spectroscopy, Dover Pub. New York
 Tubbs A.D., Wolfe A.M., 1980, ApJ 236, L105
 Ueno S., Koyama K., Nishida H., Yamauchi S., Ward M.J., 1994, ApJ 431, L1

van Dishoeck E.F., Black J.H., 1987, *Physical Processes in Interstellar Clouds*, eds. G.E. Morfill, M. Scholer, Reidel Publishing Company, p. 241
 van Ojik R., Röttgering H.J.A., Miley G.K., Hunstead R.W., 1997, *A&A* 317, 358
 Varshalovich D.A., Potekhin A.Y., 1996, *Astron Letters* 22, 1
 Wiklind T., Combes F., 1997, *A&A* in press
 Wiklind T., Combes F., 1996b, *A&A* 315, 86
 Wiklind T., Combes F., 1996a, *Nature* 379, 139
 Wiklind T., Combes F., 1995, *A&A* 299, 382
 Wiklind T., Combes F., 1994b, *A&A* 288, L41
 Wiklind T., Combes F., 1994a, *A&A* 286, L9
 Wilson T.M., Matteucci F., 1992, *A&AR* 4, 1

7. Appendix

Here we present in more detail the use of molecular rotational lines as a probe of the invariance of physical constants over large spatial and temporal scales. In particular, we show that there is a limit to the accuracy of molecular rotational lines, coming from our incomplete solution of the Schrödinger wavefunction for a complex system such as a molecule.

7.1. A diatomic rigid rotator

As a first approximation we will look at a diatomic molecule without considering the centrifugal distortion and the zero-point vibrational energy.

The energy of a rotational level J is

$$E_{\text{rot}} = \frac{\hbar}{4\pi I} J(J+1), \quad (11)$$

where J is the angular momentum quantum number and I is the molecular moment of inertia about axes perpendicular to the internuclear axis (cf. Townes & Schawlow 1975). For a diatomic molecule the moment of inertia can be expressed as μr_e^2 , where μ is the reduced mass of the two atoms and r_e is the equilibrium intranuclear distance of the two atoms. To within a factor of 2–3, we can set $r_e \approx a_0$, the Bohr radius. Expressed in fundamental parameters⁴, the energy of a rotational level J is

$$E_{\text{rot}} \approx \left(\frac{c^2}{2\hbar} \right) \frac{m_e^2 \alpha^2}{\mu} J(J+1), \quad (12)$$

where m_e is the electron mass and α the fine structure constant. The frequency of a rotational transition following the selection rule $\Delta J = \pm 1$ is

$$\nu = \frac{2\hbar}{4\pi I} (J+1) \approx \left(\frac{c^2}{h} \right) \frac{m_e^2 \alpha^2}{\mu} (J+1). \quad (13)$$

This gives the correct frequency of a transition to within a factor of a few. The discrepancy arises from the approximation of the effective internuclear separation as the Bohr radius, but does not affect the analysis of the fundamental physical parameters. A shift in the line frequency due to changes in the

reduced mass μ , the electron mass m_e and the fine structure constant α is therefore

$$\frac{\Delta\nu}{\nu} = \sqrt{\left(\frac{\Delta\mu}{\mu} \right)^2 + 4 \left(\frac{\Delta m_e}{m_e} \right)^2 + 4 \left(\frac{\Delta\alpha}{\alpha} \right)^2}. \quad (14)$$

If the redshift of an object causing the observed transition is known apriori, we can directly relate the shift in frequency or, similarly, in velocity $\Delta v = c\Delta\nu/\nu$ to combined changes in the three parameters μ, m_e and α . In order to measure a shift of 1 km s^{-1} , we must have $\Delta\mu/\mu \sim 3 \times 10^{-6}$ (if $\Delta m_e = \Delta\alpha = 0$). However, any determination of a redshift involves a measurement of line radiation, with the possibility of being affected by changing physical parameters (not necessarily the same as for molecular rotational transitions). Hence, we must make a ‘differential’ measurement in order to test their invariance. In the case of a rigid diatomic molecule, this is done by comparing two different species. What we measure is two ratios of frequencies; the ‘laboratory’ (called *lab*) and the observed frequency (called *obs*):

$$\frac{\nu_{\text{lab}}}{\nu_{\text{obs}}} = 1 + z. \quad (15)$$

For two different molecules a and b , we can now write:

$$1 - \frac{\left[\frac{\nu_{\text{lab}}}{\nu_{\text{obs}}} \right]_b}{\left[\frac{\nu_{\text{lab}}}{\nu_{\text{obs}}} \right]_a} = \frac{\Delta z}{1 + z_a}. \quad (16)$$

Since we are comparing two molecular species at two different epochs, the electron mass and the fine structure constant will drop out and we have

$$\frac{\Delta z}{1 + z_a} = \frac{\Delta R_\mu}{R_{\mu_0}} \quad (17)$$

$$\Delta R_\mu = \left(\frac{\mu_b}{\mu_a} \right)_0 - \left(\frac{\mu_b}{\mu_a} \right)_z \quad (18)$$

$$R_{\mu_0} = \left(\frac{\mu_b}{\mu_a} \right)_0. \quad (19)$$

In Eqs. 20–22 we use 0 as a subscript for mass ratios obtained in the laboratory ($z=0$) and z for mass ratios at a distant epoch. Comparison of molecular rotational transitions are thus sensitive to the strong force only, affecting the proton and neutron masses. For practical purposes, the largest effect is obtained when R_{μ_0} is small, i.e. $\mu_a \gg \mu_b$.

7.2. Non-rigid diatomic molecules

The next step in the complexity of a diatomic molecule is the centrifugal distortion and the zero-point vibrational energy. As the rotational quantum number J increases the molecule rotates faster and the internuclear separation increases. This leads to a larger moment of inertia and a decrease in the energy compared with the rigid rotator. The zero-point vibrational energy introduces a periodic oscillation in the internuclear separation, affecting the moment of inertia and the energy levels.

A separate treatment of the atoms and the electrons (the Born–Oppenheimer approximation) is necessary in order to describe the total potential in such a way that the Schrödinger

⁴ These are usually called ‘constants’, but since we are testing their invariance, we will refer to them as ‘parameters’.

wave function can be solved. Ultimately, as we will discuss in the next subsection, the Born–Oppenheimer approximation puts a limit to the accuracy with which molecular rotational transitions can be used to test the invariance of physical parameters.

Dunham (1932, Phys Rev 41, 721) gave the vibrational and rotational energy levels for any potential which can be expanded in powers of $(r - r_e)$ (see also Townes & Schawlow 1975). However, we will use the simpler Morse potential in order to emphasize the dependence on fundamental physical constants. The Morse potential is written

$$U(r) = D(1 - \exp(-a(r - r_e)))^2, \quad (20)$$

where D is the dissociation energy of the molecule, r_e is the equilibrium intranuclear separation and a is a constant. The frequency of a rotational transition ($v = 0$) becomes

$$\nu = 2B_e(J + 1) - 4D_e(J + 1) - \alpha_e(J + 1) \quad (21)$$

$$B_e = \frac{\hbar}{4\pi I_e} \approx \left(\frac{c^2}{2h}\right) \frac{m_e^2 \alpha^2}{\mu} \quad (22)$$

$$D_e = \frac{8\pi^2 \mu B_e^3}{a^2 D} \approx \left(\frac{\pi^2 c^6}{a^2 D h^3}\right) \left(\frac{m_e^3 \alpha^3}{\mu}\right)^2 \quad (23)$$

$$\alpha_e = \left(\frac{3c^3}{\sqrt{32D\pi h}}\right) \left(\frac{m_e \alpha}{\mu^{1/2}}\right)^3 \left[1 - \frac{\hbar}{acm_e \alpha}\right] \quad (24)$$

$$. \quad (25)$$

If we for simplicity disregard the zero-point vibrational energy, we can write the line frequency as

$$\nu = \left(\frac{c^2}{h}\right) \frac{m_e^2 \alpha^2}{\mu} (J + 1) \left[1 - \left(\frac{c^3}{a^2 D h^2}\right) \frac{m_e^3 \alpha^3}{\mu} (J + 1)^2\right] \quad (26)$$

The first term is identical to that obtained for the rigid rotator and the second term is the effect of centrifugal stretching (lowering the frequencies). Due to this term, the dependence on m_e and α at $z = 0$ and at z does not cancel when comparing the redshifts for two molecules a and b , as was the case for the rigid rotator. Hence, $\Delta z/(1 + z)$ depends on all three parameters; μ , m_e and α . For low J -values, however, the dependence on the electron mass and the fine structure constant is small, and the rigid rotator represents a good first order approximation. The nonlinear dependence on J in the centrifugal distortion means that it is possible to compare the redshifts derived from different rotational transitions of the same molecule.

7.3. Limitations to the accuracy

As discussed in Sect. 5.4, the accuracy of using comparative measures of redshifts derived from either different emission mechanisms (optical, 21 cm hyperfine line, molecular rotational lines, etc) is limited by velocity gradients in the emitting medium and the fact that different gas masses contribute differently to the various emission/absorption processes. This is a grave concern also when using molecular rotational transitions, even when the same molecular species is used, but with different J levels. However, even if this was not the case, the accuracy is limited by our inexact quantum mechanical description of a molecule.

There are two main uncertainties which affect a test of the invariance of fundamental physical parameters. The first is anharmonicity of the potential. This is particularly true for the Morse potential used here. The situation is improved somewhat by using the method of Dunham (cf. Townes & Schawlow 1975), but the method involves parameters which can be calculated from spectroscopically observable quantities and they ultimately put a limit to how accurate the ratio of two reduced masses can be calculated to $\sim 10^{-7}$ (Townes & Schawlow 1975). The second uncertainty involves the Born–Oppenheimer approximation, where the electronic and atomic contributions to the total potential are treated separately. Although electrons can be considered to be more or less spherically distributed around their respective nuclei, and thus not contributing to the moment of inertia (the so called ‘slip effect’), electrons in the valence shell will give a contribution to the moment of inertia of $\sim n_e m_e r^2$, where n_e is the number of electrons in the valence shell, m_e is the electron mass and r is an average radius from the nucleus with which the valence shell is associated. This contribution to the moment of inertia is very small indeed, but when deriving mass ratios it limits the accuracy to $\sim 10^{-6}$ (smaller for heavy molecules and larger for lighter ones). An effect which is closely related to the valence electrons is so called L–uncoupling. Rotation tends to excite the valence electrons from their ground $^1\Sigma$ state with zero angular momentum, to excited $^1\Pi$ states, with unit angular momentum. This in itself affects the rotational energy, but a larger effect comes from the fact that the Π state also produces a large magnetic field at the positions of the nuclei. This induces magnetic hyperfine interaction, again changing the rotational energy levels. This L–uncoupling can be measured in the laboratory and is found to introduce uncertainties of $\sim 10^{-6}$ in estimated mass ratios (Townes & Schawlow 1975).

Hence, the uncertainties associated with estimates of mass ratios of molecules is of the order 10^{-6} . This value is of the same order as the $\Delta\mu/\mu$ necessary to produce a shift of $\sim 1 \text{ km s}^{-1}$ relative to the ‘true’ redshift of a molecular rotational line. Smaller shifts than this will therefore not be useful in testing the invariance of physical parameters.